mCBM@SIS18

The CBM Collaboration

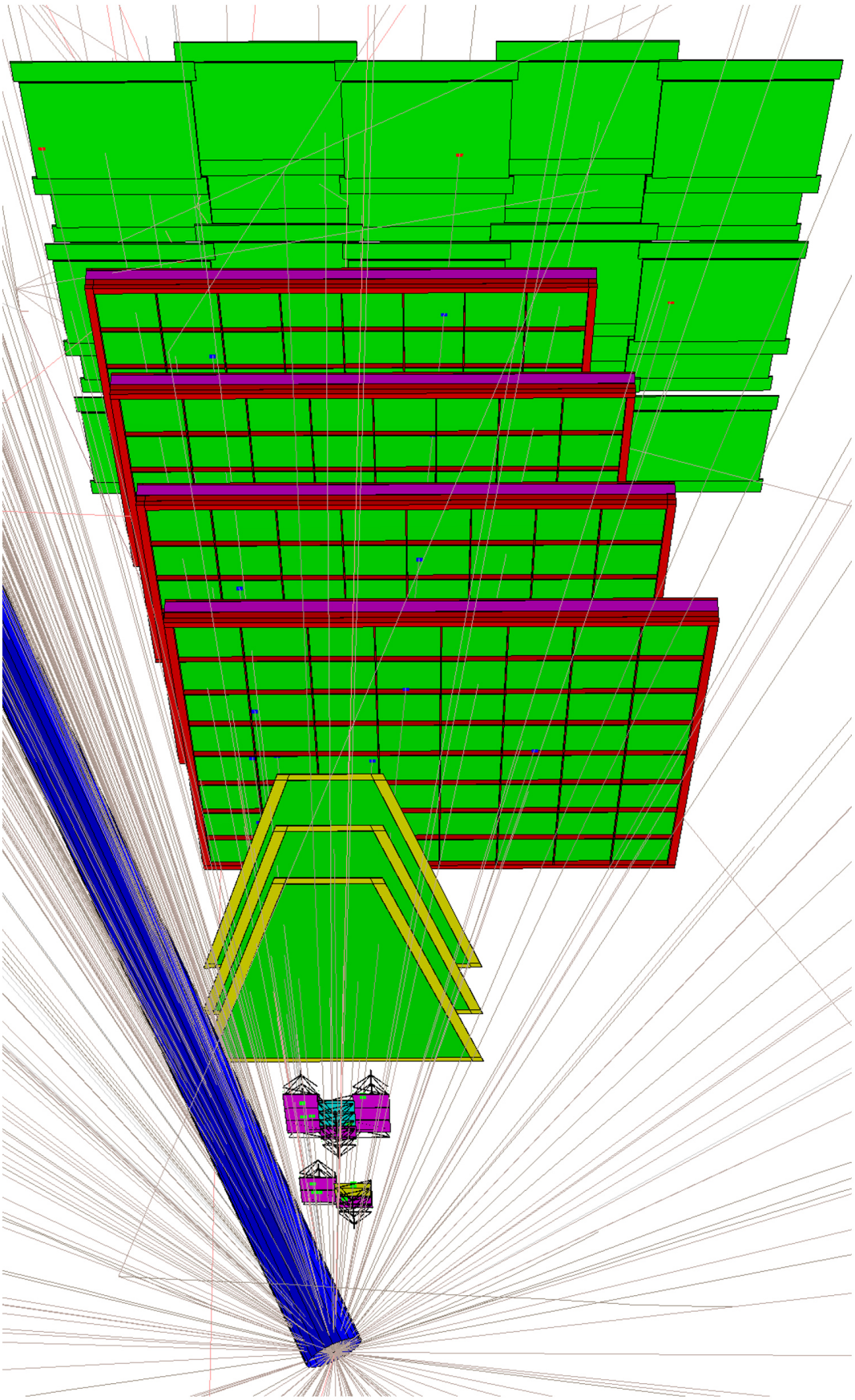

Compressed Baryonic Matter Experiment

Beamtime Application

mCBM@SIS18

A CBM full system test-setup for high-rate nucleus-nucleus collisions at GSI / FAIR

The CBM Collaboration

Submitted to the
General Program Advisory Committee (G-PAC) of GSI / FAIR
June 19^{th}, 2017

The mCBM working group and the CBM Collaboration

The mCBM working group comprises participants from the CBM Collaboration[1] and cooperating institutes:

GSI Helmholtz Center for Heavy-Ion Research GmbH (GSI), Darmstadt, Germany
D. Emschermann, V. Friese, P.-A. Loizeau, W. Niebur, A. Senger, C. Sturm[2], F. Uhlig.

Frankfurt Institute of Advanced Studies (FIAS), Frankfurt am Main, Germany
J. de Cuveland.

Physikalisches Institut, Ruprecht-Karls-Universität Heidelberg, Germany
N. Herrmann.

The CBM detector subsystems

MVD	Micro Vertex Detector
STS	Silicon Tracking System
MUCH	MUon CHambers
TRD	Transition Radiation Detector
TOF	Time-Of-Flight System
RICH	Ring Imaging CHerenkov detector
PSD	Projectile Spectator Detector
ECAL	Electromagnetic CALorimeter

are represented by their individual project leader.

[1] The current list of CBM members is provided in Appendix D
[2] Project leader mCBM (designated)

Executive summary

We propose a full-system test-setup for the Compressed Baryonic Matter experiment CBM at SIS18 under the name *mCBM@SIS18* ("mini-CBM", later shortened to "mCBM"), comprising final prototypes or pre-series components of all CBM detector subsystems. The primary aim is to study, commission and test the complex interplay of the different detector systems with the free-streaming data acquisition and the fast online event reconstruction and selection. In particular, it will allow to test the detector and electronics components developed for the CBM experiment as well as the corresponding online/offline software packages under realistic experiment conditions up to top CBM interaction rates of 10 MHz.

Commissioning and operating mCBM in 2018 and 2019 will prove the proper functioning of the detectors as well as the read-out electronics before the final series production starts. The experiences gathered during the operation of the complete mCBM campaign will be of highest value to minimize the commissioning time for the full CBM experiment at SIS100.

With mCBM, the ambitious detector sub-systems, readout and data processing concept of CBM will be validated on the base of a benchmark observable, namely the Λ production yield in $\mathrm{Au} + \mathrm{Au}$ and $\mathrm{Ni} + \mathrm{Ni}$ collisions at top SIS18 energies, which can be compared to published data. The feasibility has been successfully demonstrated by performing Monte-Carlo simulations including GEANT geometries of all mCBM detector subsystems and full detector response.

Application for beam time

The beamline to HTD and the HTD cave shall be basically prepared in 2017 while the mCBM test-setup shall be installed and commissioned in the years 2018 and 2019. Hence, we apply for 81 shifts with parasitic beam and 6 shifts as main user in this period.

For 2020 and 2021, we intend high-performance benchmark runs. We expect that these runs will produce new data on sub-threshold Λ-production at SIS18 energies which will be published in scientific journals. For this program we anticipate a need of about 30 shifts as main user and preparatory phases with 30 shifts as parasitic user.

Contents

1 Motivation

The Compressed Baryonic Matter experiment (CBM) is one of the major experimental projects at the upcoming FAIR facility. It will explore strongly interacting matter at highest net-baryon densities by investigating nucleus-nucleus collisions in fixed-target mode with extracted beams from the SIS-100. The unique feature of CBM is its high-rate capability of up to 10^7 interactions per second, which will make it sensitive to extremely rare probes and, consequently, will give it a high discovery potential. In order to achieve these ambitious goals, CBM will employ fast and radiation-hard detectors and readout electronics. Moreover, a novel, free-streaming data acquisition system will be used, which aggregates the data sent by the self-triggered front-end electronics and push them to an online compute farm for data reconstruction and selection in real time. The described high-performance read-out hardware needs high-performance firmware for the FPGA layers of the data acquisition system as well as software for a fast and highly parallel on-line track and event reconstruction and selection. Measuring nucleus-nucleus collisions at unprecedented collision rates the interplay of these complex, high-performance hard- and software components presents a challenge.

By today, the design of the detector and electronics components for CBM is largely completed, and series production is going to start. The components were tested in the laboratory and in beam. However, it is highly desirable to test and optimize the operation of the full system of complex hard- and software components – from the detectors over the readout ASICs and the DAQ to on- and offline data processing and analysis – under realistic experiment conditions before the installation and commissioning of the full CBM detector setup.

We thus propose a full-system test for CBM at the GSI/FAIR host lab site in the years 2018 - 2021 under the name *mCBM@SIS18* ("mini-CBM", later shortened to mCBM). The test setup shall include detector modules from all CBM detector subsystems (MVD, STS, RICH, MUCH, TRD, TOF, ECAL)[3], using (pre-)series production specimen, positioned downstream of a nuclear target at an angle of 25° with respect to the beam axis. The concept is sketched in Fig. 1. A PSD prototype at zero degrees will be used to characterize the collision geometry.

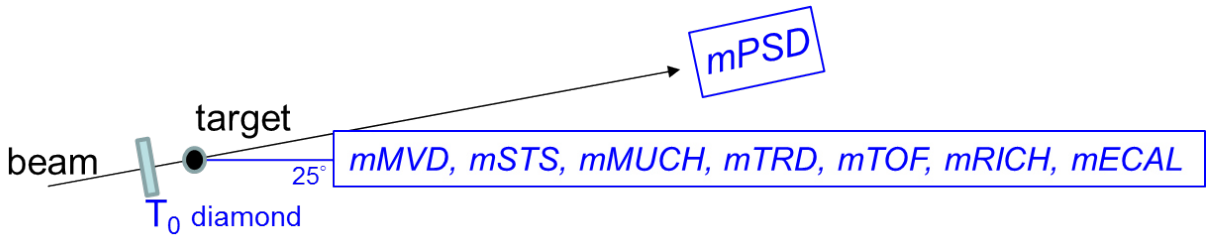

Figure 1: Concept sketch of the proposed mCBM test-setup. The compact setup measures in length about 3 m and is positioned under 25° with respect to the primary beam. It does not comprise a magnetic field. The foreseen installation site is the detector test area HTD of the SIS18 facility, at the entrance to the experimental area HTC hosting the R^{3}B experiment.

[3]MVD: Micro Vertex Detector, STS: Silicon Tracking System, MUCH: MUon CHambers, TRD: Transition Radiation Detector, TOF: Time-Of-Flight stop wall, RICH: Ring Imaging CHerenkov detector, PSD: Projectile Spectator Detector, ECAL: Electromagnetic CALorimeter, see [3] - [7]

Hence, the mCBM setup will allow to test and optimize

— the operation of the detector prototypes in a high-rate nucleus-nucleus collision environment,

— the free-streaming data acquisition system including the data transport to a high-performance computer farm located in the Green IT Cube,

— the online track and event reconstruction as well as event selection algorithms,

— the offline data analysis and

— the detector control system.

Commissioning and running mCBM in the first two years will complete our knowledge on proper functioning as well as on the performance of the CBM detector systems and their associated Front-End Electronics (FEE) before the final series production starts. With a benchmark (physics) observable – the production multiplicity of Λ baryons – the proper functioning of the entire experimental chain will be verified by comparing to published data. The experiences obtained during the complete mCBM campaign will significantly reduce the commissioning time for the full CBM experiment at SIS100.

2 The mCBM experiment

2.1 Setup

The detector subsystems of the mCBM test setup will be positioned downstream a solid target under a polar angle of about 25° with respect to the primary beam, enclosed in a beam pipe towards a beam dump located 7 m downstream at the south end of the experimental area.

The presented design focuses on the system performance aspect integrating existing (or currently under construction) prototype modules of all CBM detector subsystems into a common, high-performance free-streaming data acquisition (DAQ) system. As for the Compressed Baryonic Matter (CBM) experiment, a First Level Event Selector (mFLES) will be used to filter the data stream. According to the needs, the initial configuration of the mCBM test-setup is rather versatile and can be variably adapted. mCBM also facilitates detailed high counting rate tests for CBM detector components or Front-end Electronics (FEE) that are currently in the final development phase before the series production starts. Detector stations of CBM subsystems which will be available for the mCBM test-setup are given in Table 1, labeled with a prefix "m".

mSTS	2x small STS prototype stations bearing 2 x 2 and 3 x 3 modules. The 1^{st} station consists of two and the 2^{nd} of three half-ladders. In total 13x silicon strip sensors, each with a size of 6 x 6 cm^2 and 1024 channels on each sensor side. More than 26k readout channels in total. To be readout with 26x STS-XYTER FEB-8x1, interfaced to the GBTx ROB-3.
mMUCH	3x GEM prototype stations consisting of M2 modules with 2304 pads. Each module is equipped with 18x MUCH-XYTER FEBs, interfaced to the GBTx ROB-3. Almost 7k readout channels are available in total.
mTRD	4x TRD prototype modules, type 8. Each 95 x 95 cm^2 large, with 768 rectangular pads, 6x FEB-4x1-2 per module interfaced to the GBTx ROB-3. More than 3k readout channels in total.
mTOF	5x TOF M4 prototype modules each containing 5 MRPC counters (32 x 27 cm^2). The readout will be performed with PADI and GET 4 electronics interfaced to the GBTx ROB-1 as used in FAIR phase 0 at STAR. In total 1600 readout channels.
mRICH	4x RICH solid-state-modules (glass or quartz radiator), equipped with 4x12 MAPMTs and 2 DiRICH modules. The interface to the mCBM DAQ needs to be developed.
mPSD	8x PSD modules, already tested in beam at CERN PS in 2017, additional beam test at CERN in 2018, available in 2019. The interface to the mCBM DAQ needs to be developed.
mECAL	A small calorimeter of 25-49 "shashlik" like modules in a 5 x 5 or 7 x 7 matrix. The readout chain has to be developed.
mMVD	One or two stations close to the target, employing a future generation of the CBM pixel sensor MIMOSIS. The first full-size version of this sensor becomes available in 2019. The interface to the mCBM DAQ needs to be developed.

Table 1: Detector stations of CBM detector subsystems which will be available for the mCBM test setup.

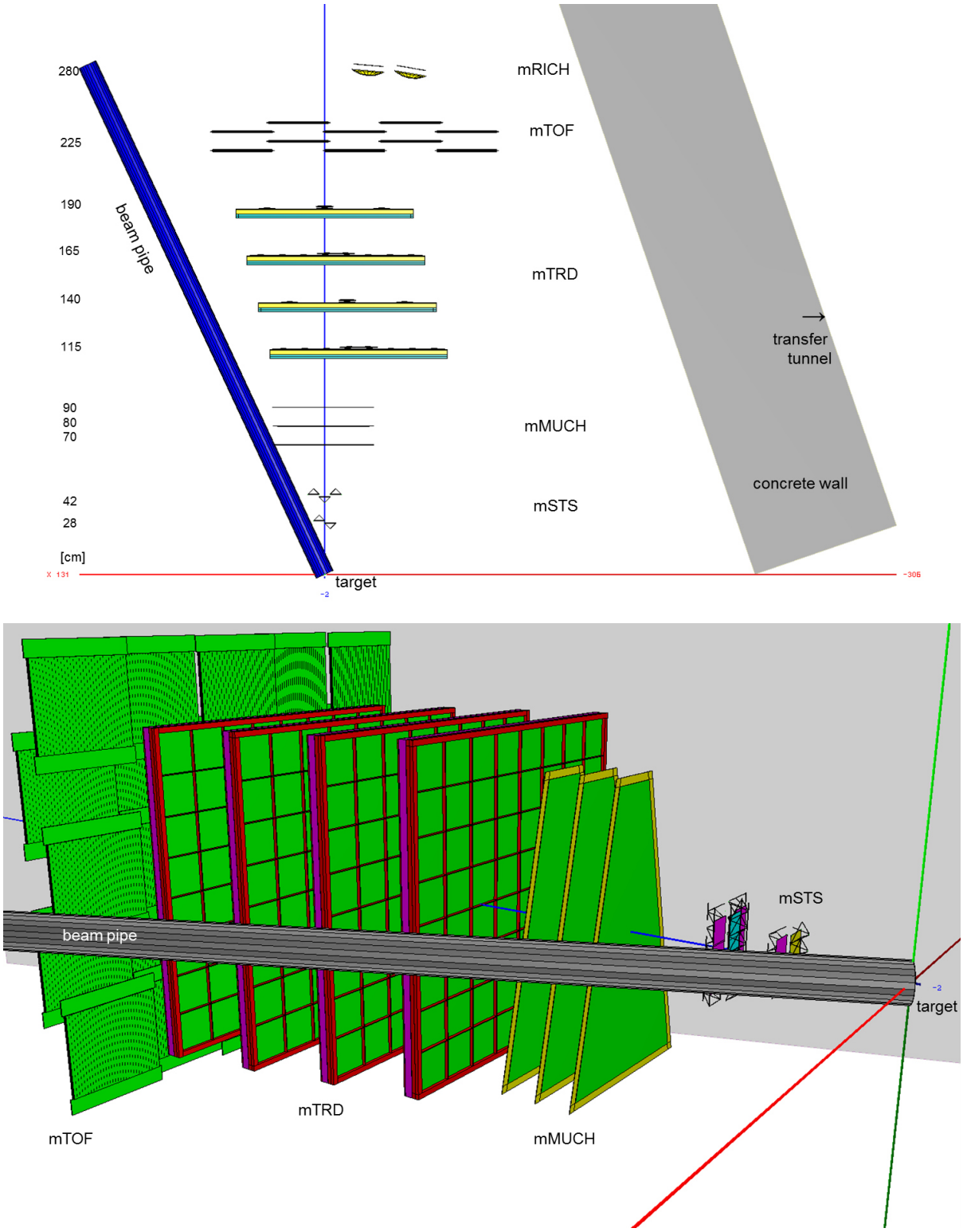

Figure 2: Top view (top panel) and side view (bottom panel) of the mCBM test setup at the HTD cave. The detector stations are aligned at an emission angle of about $\Theta_{lab} = 13^{\circ}$ (beam pipe side) at y = 0. The x-, y- and z-axes are respectively plotted as red, green and blue colored lines. The beam pipe is located in the x-z plane, at positive x-coordinates and an angle of 25° with respect to the z-axis. Note, the GEM counters of the mMUCH subsystem are trapezoidal shaped (see lower panel), which is not visible in the top-view projection.

Like for the full CBM experiment, mCBM uses a right-handed coordinate system, the origin of which is located in the target position, see Fig. 2. The x-axis (red) is horizontally aligned, the y-axis (green) is pointing vertically upwards, the z-axis (blue) is also horizontally oriented, but rotated around the y-axis by -25 ° away from the direction of the primary beam. The beam pipe downstream of the target is therefore located in the x-z plane, at positive values of x and z. Except for mRICH, all detector subsystems are aligned in the x-y plane, orthogonal to the z-axis. The two mSTS stations and the 4^{th} layer of mTRD are centered in x and y. Histograms matching the active detector area in the x-y plane (see Fig. 3), are shown in the perspective of an observer positioned downstream of the mCBM setup and looking into the upstream direction, towards negative z-coordinates. This representation is identical to the one for the full CBM experiment.

As shown in Fig. 2, the test-setup does not comprise a magnetic field, and, therefore, will measure charged particles produced in nucleus-nucleus collisions traversing the detector stations following straight trajectories. On the side of the beam pipe the detector stations are aligned at an (horizontal) emission angle of about $\Theta_{lab} = 13^{\circ}$ (at y = 0), see Tab. 2. For tracks passing the active area of the mSTS, mMUCH, mTRD and mTOF subsystems the covered Θ_{lab} range results to $13^{\circ} - 37^{\circ}$. The overall acceptance is limited by the mSTS, which is located very close to the beam pipe and cannot be moved further upstream.

The tracking system comprises 2x STS (mSTS), 3x MUCH (mMUCH) and 4x TRD stations (mTRD) in total 9x tracking layers which provide redundant position information and allow to perform tracklet searches. The setup will possess a high-resolution time-of-flight system consisting of a fast and segmented diamond counter for time-zero (t_0) determination in front of the target as well as a TOF stop wall (mTOF). Four RICH solid-state-modules forming the mRICH subsystem will be placed behind the mTOF detector and deliver a second measurement of the particle velocity in a selected acceptance window. A small calorimeter (mECAL) will also be mounted behind the mTOF covering a reduced acceptance. Additionally, 8x PSD prototype-modules (mPSD) will be used to characterize the collision geometry. In a later stage MVD stations (mMVD) will be included into the test-setup enabling a high-precision vertex reconstruction. Detailed descriptions of the mCBM subsystems are given in appendix A.

subsystem station	covered horizontal angular range	covered vertical angular range	position on z-axis	comment
mSTS 0	$13.0^{\circ} - 37.0^{\circ}$	$\pm 12.0^{\circ}$	28 cm	1^{st} station
mSTS 1	$13.0^{\circ} - 37.0^{\circ}$	$\pm 12.0^{\circ}$	42 cm	2^{nd} station
mMUCH 1	$13.1^{\circ} - 36.9^{\circ}$	$\pm 11.9^{\circ}$	80 cm	2^{nd} station (at y=0, trapezoidal shape)
mTRD 3	$11.4^{\circ} - 38.6^{\circ}$	$\pm 13.6^{\circ}$	190 cm	last (4^{th}) station
mTOF	$11.1^{\circ} - 46.6^{\circ}$	$\pm 15.3^{\circ}$	225 cm	not centered in x

Table 2: Overview of the geometrical acceptance of the mCBM subsystems. The mCBM subdetector stations are numbered starting from 0. Some of the detector layers (mTRD 0, mTRD 1, mTRD 2 and mTOF) were shifted in -x direction to limit the hit rates on active detector components, at small angles, outside the mCBM setup acceptance.

Extensive Monte Carlo simulations have been performed to extract numbers like multiplicity of charged tracks or hit multiplicities and hit rates in the different detector stations. As input, events for minimum-bias Au + Au collisions at 1.24 AGeV have been generated with the UrQMD transport code. The complete mCBM geometry as shown in Fig. 2 has been implemented in CbmRoot and used for GEANT3 particle transport simulations. Within the mCBM acceptance

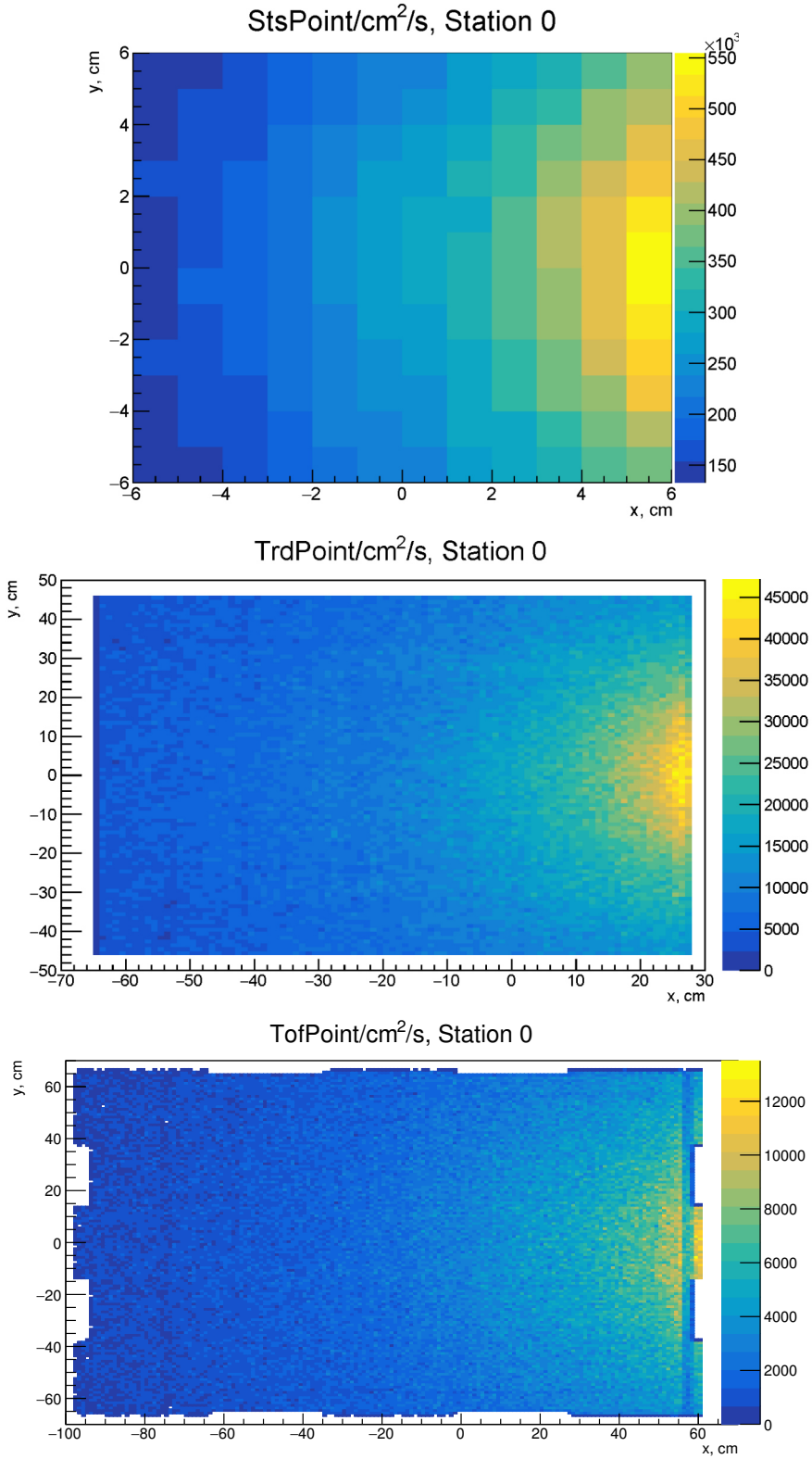

Figure 3: Hit rates (z-axis, hits per cm^2 per second) inside the first STS (top), first TRD station (middle) and inside the TOF stop wall (bottom) obtained in Au + Au minimum-bias collisions at 1.24 AGeV (simulation input: UrQMD). The hit rates are normalized to 10^7 collisions per second. Note, the beam traverses the detector stations at large positive x-values. The vertical band visible in the TOF hit rate (bottom) at x = 57cm is caused due to shadowing by the overlap of the aligned outer frames of the four mTRD modules located upstream of mTOF.

an average charged-track-multiplicity of about 5 has been obtained in minimum-bias and about 30 in central Au + Au collisions. In Fig. 3 hit rates normalized to 10^7 collisions per second are shown which have been obtained inside the first STS (top) and first TRD station (middle) as well as in the TOF stop wall (bottom).

2.2 Data acquisition and data transport

The CBM experiment at FAIR will measure relativistic nucleus-nucleus collisions with collision rates up to 10 MHz leading to data rates up to 1 TB per second. To achieve the required performance a free-streaming data acquisition system is being developed including ultra-fast and radiation-tolerant ASICs as front-end chips followed by CERN GBTx-based radiation-tolerant data aggregation units. Further down-stream, the data streams are handled by Data Processing Boards (DPB) containing powerful FPGAs and are forwarded via FLES Input Boards (FLIB), a PCIe based FPGA board, to a large-scale computer farm, the First-Level Event Selector (FLES), which performs on-line event selection, see Fig. 4. The described high-performance readout hardware needs high-performance firmware for the FPGA layers up to a fast and highly parallel on-line track and event reconstruction and analysis software.

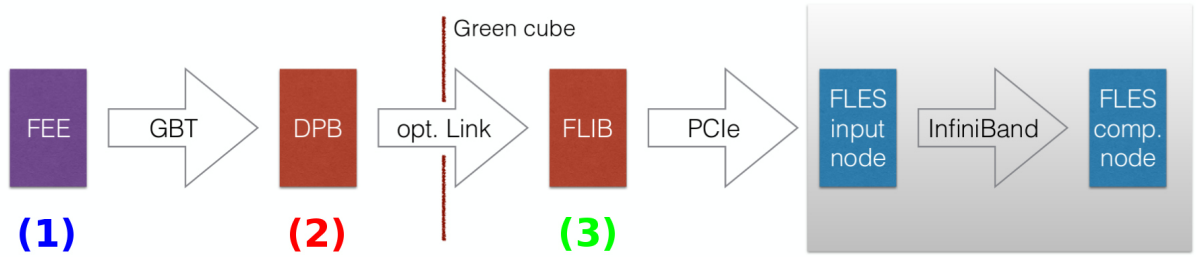

Figure 4: Envisaged mCBM readout chain for the startup phase, based on DPB and FLIB. The mCBM subsystems installed in the cave (1) are equipped with individual front-end electronics. These front-ends are interfaced by the GBTx ASIC, which forwards the detector data via optical GBT link. All GBT links are received by the DBP layer located at 50 m distance in the DAQ container (2). The DPB is a FPGA based board which allows for subsystem specific pre-processing of the arriving data stream. A long distance optical link connects the DPB output to the FLIB board installed in the FLES input node in the Green IT Cube (3). The FLIB transports the arriving data in micro-slice format into the the memory of the FLES input node. An InfiniBand network links the FLES input nodes to the FLES compute nodes. Upon reception in a FLES compute node the micro-slices originating from all active subsystems are grouped into larger time-slices. These time-slices are then used for the online data reconstruction.

component	description	FPGA type	current prototype
DPB	Data Processing Board	Kintex-7	AFCK
FLIB	FLes Interface Board	Kintex-7	HTG-K700 PCIe
CRI	Common Readout Interface	Zynq UltraScale+	HTG-Z920 PCIe (planned)

Table 3: Overview of the main CBM DAQ components and their implementation.

The mCBM detector front-ends are time-synchronized to the nanosecond level by the Timing and Fast Control (TFC) system. The detector front-end digitizes signals above threshold and assigns a time stamp to the hit. This data is then forwarded via an electrical connection to the GBTx readout board, where the electrical signals acquired through a large number of e-links are

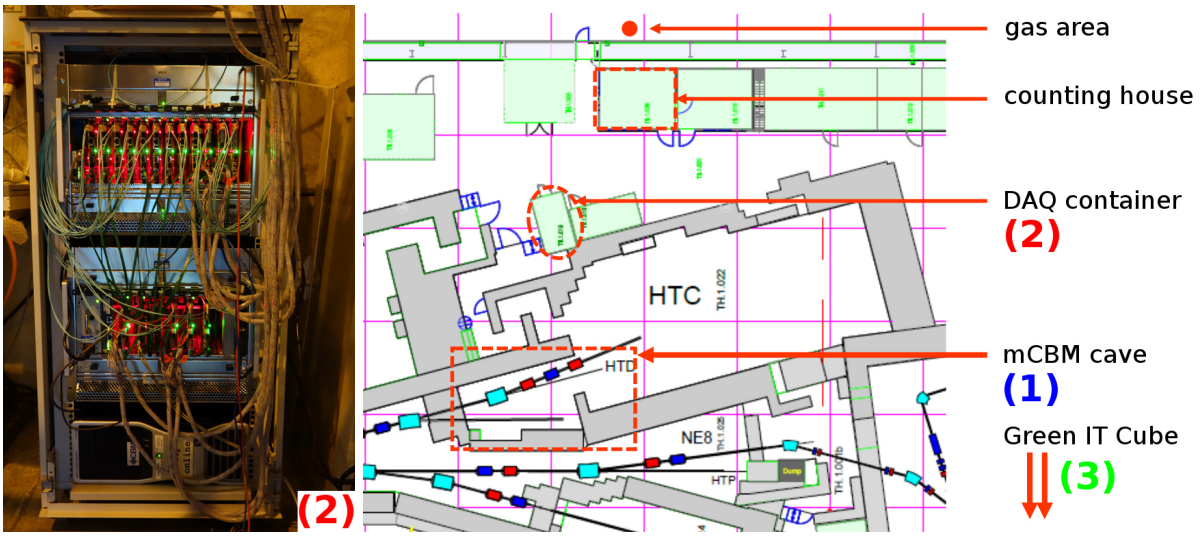

Figure 5: (right) Location of the mCBM readout chain components: the experimental setup, equipped with front-end electronics and the GBTx readout boards, will be located in the mCBM cave (1). The DAQ container (2), which will house the MicroTCA crates equipped with AFCK boards, is about 50 m away. The FLES input nodes, equipped with FLIB prototypes, and the FLES compute stage will be located some 400 m away in the Green IT Cube (3). (left) The data-processing stage of the free-streaming DAQ system, consisting of 2 MicroTCA crates equipped with AFCK boards, as used during the CERN SPS beam test in November 2016, will be installed in (2).

converted and merged into an optical GBT link operating at 4.48 Gbit/s. These GBT links are the detector interface to the Data AcQuisition (DAQ) chain.

The mCBM DAQ system will be deployed in two phases. During phase I, the GBTx-based subsystems (mSTS, mMUCH, mTRD and mTOF) will be read out using already available readout chains based on existing prototype implementations of DPB and FLIB, see Fig. 4. As current prototype hardware, an AMC FMC Carrier Kintex (AFCK) board is used for the DPB, a HiTech Global HTG-K700 PCIe board for the FLIB. Both boards are based on a Xilinx Kintex-7 FPGA. In phase II, DPB and FLIB will be replaced by a prototype of the Common Readout Interface (CRI) in the FLES input stage, as it is foreseen for the CBM experiment. In addition the mCBM subsystems (mRICH, mPSD) readout with FPGA TDCs chains will be added to the DAQ setup in 2019. For details concerning the CBM readout system and its upgrade to the CRI, please refer to appendix A.9.

2.3 Data processing

The CBM data readout concept, not employing any hardware trigger, will push all detector raw data to the online compute cluster. For high interaction rates, the raw data volume has to be reduced by more than two orders of magnitude by online selection of physically interesting data. This necessitates a partial reconstruction of the data in real-time up to a stage where a decision on some physics trigger signature can be done.

It is one of the prime aims of mCBM to test and validate the data processing concept and the reconstruction software which are being developed for the full CBM experiment. mCBM thus will be a demonstrator for the computing concept of CBM, including the reconstruction of events and selection of data in real-time and the full offline data analysis. It is thus planned to use already existing software components as far as possible for both online and offline computing in mCBM.

The interface to the reconstruction is a time-slice as a container of raw data within a given time interval. The time-slice will be built on the FLES compute nodes, where they are available for further online processing, or should be sent (in minimum-bias mode without online data selection) directly to file storage. For offline reconstruction and analysis, the raw data will be imported into the CbmRoot framework, applying the necessary calibration corrections. The first step in reconstruction is local cluster and hit finding in STS, MUCH, TRD and TOF. The corresponding software is already available (STS, TOF) or being developed (MUCH, TRD) and can be used in mCBM without modifications compared to the full CBM. Track finding will connect hits in the various sub-systems to a straight-line trajectory. For this task, the existing CBM tracking algorithms will be used in mCBM after slight modifications with respect to the straight-line track model. Event identification in the data stream will be tested both on the raw data level (before reconstruction) or after track finding on the basis of reconstructed tracks. A higher-level analysis will operate on defined events corresponding to beam-target interactions. For the analysis of the benchmark observable Λ, the KFParticle package developed for CBM will be used.

mCBM shall also demonstrate the feasibility to detect signatures of rare observables online and select data accordingly for storage. The benchmark case for online data selection at highest interaction rates is the Λ baryon, which is expected to have an experimental yield of the order of 10^{-5}. The reconstruction strategy and the algorithms are identical to that used for offline data processing. It should be noted that the identification of Λ candidates is already possible with a simplified method using only STS and TOF data, i.e., without full tracking through all detector systems, as described in the following section. Only raw data corresponding to events containing a Λ candidate will be forwarded to the mass storage. For the deployment of the reconstruction on the online compute nodes, we will use the FairMQ concurrency framework developed at GSI.

3 Benchmark observable

To verify the performance of the CBM data taking concept the mCBM setup will be used to reconstruct physics observables that can be compared to published data.

A feasibility study with the mCBM setup was performed using the Λ production probability in heavy-ion collisions as a benchmark observable. At SIS18 beam energies Λ baryons are produced close to or below the free NN production threshold. Thus their production probability is rather small (see Table 5) posing a CBM-like challenge to the reconstruction and selection task.

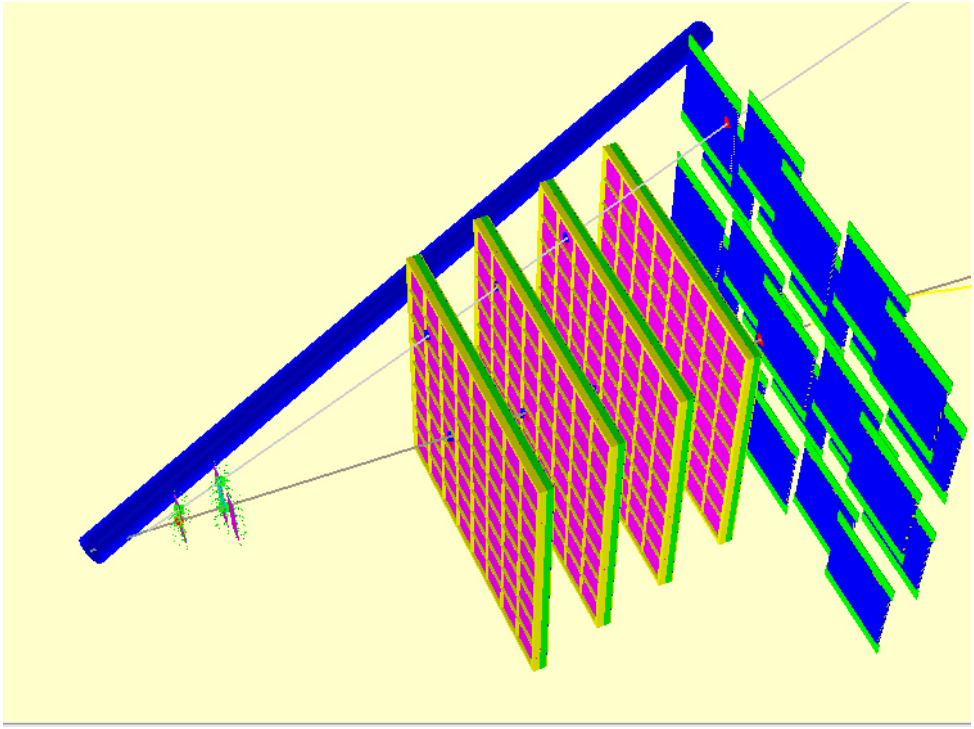

Figure 6: Illustrating the Λ-reconstruction within the mCBM setup.

Since mCBM does not include a magnetic field for momentum measurement, the reconstruction has to be done via time-of-flight (TOF) and track topology. That the limited information available is sufficient for Λ reconstruction is demonstrated by a MC simulation, modeling the full data analysis chain. The available information for a Λ decaying into a proton and a pion is visualized in Fig. 6 showing the reconstructed hits in the subsystems STS, TRD and TOF. For simplicity, only STS and TOF hits are considered for the reconstruction algorithm that proceeds in the following steps:

1. Find straight tracks originating from the primary vertex assumed to be located at (0,0,0). (Note that in the MC simulation a beam spot size of $\sigma_x = \sigma_y = 1\,\mathrm{mm}$ is assumed.) TOF hits are connected to the STS hit that is closest in transverse distance to the straight line hypothesis in the STS planes. Track candidates are only formed if the transverse distance is smaller than a selection cut value (Δd_1).

2. For the primary track candidates a hit in the other STS plane is being looked for. Its expected coordinates are calculated by a straight line hypothesis from the position of the 1. STS hit and the nominal target position. A track is formed if the transverse distance is smaller than a cut value (Δd_2). Hits attributed to this track are not used to form any other track.

3. A secondary decay proton is declared to be found among the primary track candidates when the following condition is met: the impact parameter of the straight line, defined by the two STS hits, with respect to the nominal vertex position exceeds a given cut value (Δd_{proton}) in the target plane.

4. Secondary pions are reconstructed from TOF - STS hit pairs that did not pass the Δd_1 - condition from step 1. The intercept of the line formed by these pairs with the second STS plane is used to find a second STS hit that did not pass the Δd_1 - condition either and has a distance in the STS plane to the extrapolated line position of less than the cut value Δd_{pion}.

5. Within an event proton and pion candidate pairs are formed, if the opening angle exceeds a selection value α_{min}, if the distance of closest approach is smaller than a limit (DCA_{max}) and the distance of the secondary vertex to the nominal target lies in a requested range [L_{min}, L_{max}].

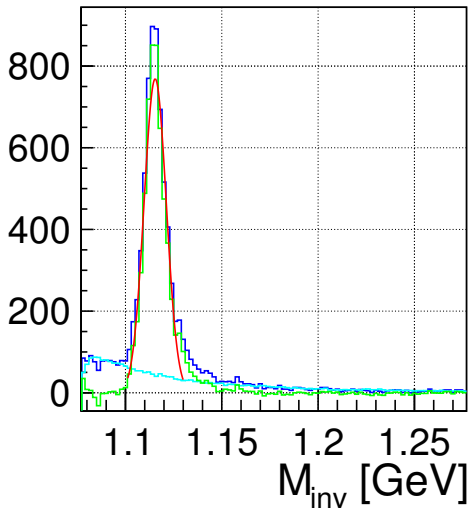

Figure 7: Λ-identification in UrQMD events in Ni + Ni collisions at 1.93 AGeV. Invariant mass distributions are shown for pair combinations (combinatorics) within events (dark blue), for pair combinations from mixed events (cyan) and for the subtracted distribution (green). Statistics information is obtained from a gaussian fit to the subtracted distribution (red line) and is summarized in Table 5.

The result of the procedure for 10^8 minimum bias UrQMD events of the reaction Ni + Ni at an incident energy of 1.93 AGeV is shown in Fig. 7. The employed selection values are summarized in Table 4. The quantitative analysis of the Λ - invariant mass peak is shown in Tab. 5.

The phase space coverage is shown in Fig. 8 demonstrating that the acceptance of mCBM is limited to a small angular range close to mid-rapidity. In this range published data are available in [1][4] that the mCBM results can be quantitatively compared to. It is worth noting that the technical goal and challenge is to reconstruct the invariant mass distributions shown in Fig. 7 and 9 within a time period of 10 s data taking at SIS18, assuming a beam intensity of 10^8 ions per second bombarded on a 10 % interaction target.

[4]Soon, there will be HADES data available on Λ production in Au + Au collisions at 1.23 AGeV, to be published.

Δd_1	1.0 cm
Δd_2	0.3 cm
Δd_{proton}	0.4 cm
Δd_{pion}	0.3 cm
α_{min}	0.1 rad
DCA_{max}	0.1 cm
L_{min}, L_{max}	5. cm, 25. cm

Table 4: Cut values used in the Λ - reconstruction. For explanation see text.

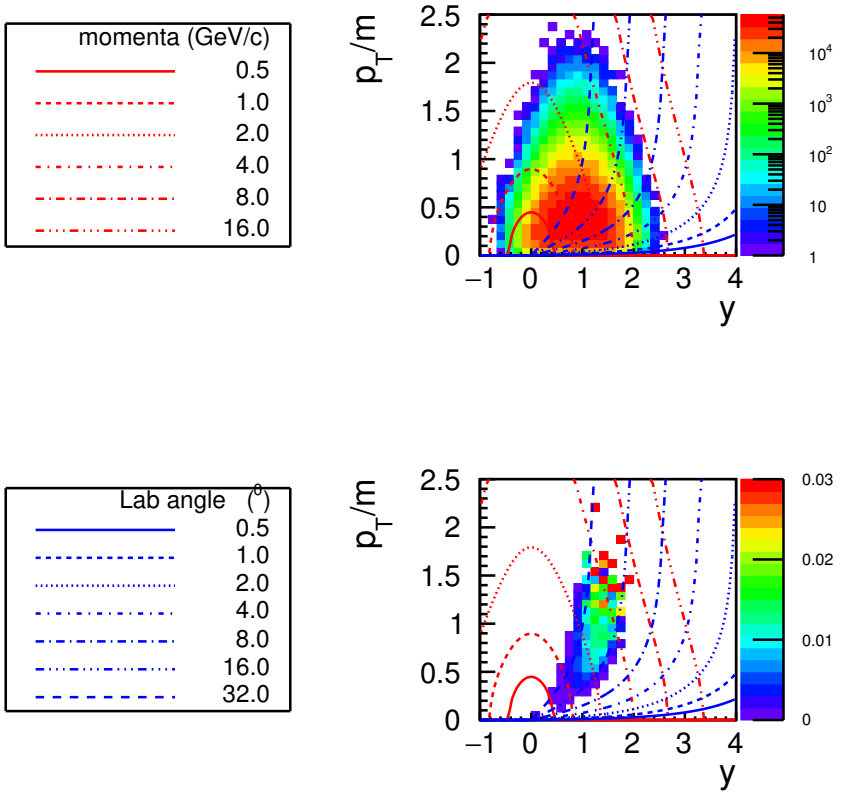

Figure 8: Phase space distribution of primary Λ - baryons produced in Ni + Ni collisions at 1.93 AGeV (top) with the UrQMD event generator and efficiency for reconstruction with mCBM using the method described in the text (bottom). Red and blue lines indicate constant laboratory momenta and laboratory polar angles, respectively. Compare to Tab. 2 for an overview of the horizontal mCBM acceptance in Θ_{lab}.

To get even closer to the load anticipated for CBM operation at SIS100 the feasibility of reconstructing Λ baryons in the heavier system Au + Au implying lower beam energies was investigated. Fig. 9 presents the results of the analysis for the reaction Au + Au at an incident beam energy of 1.24 AGeV employing the same selection cuts that were used for the Ni + Ni analysis (see Table 4). After background subtraction a clear peak is visible albeit with a much worse signal to background ratio as compared to the Ni + Ni case (see Table 5). Improvements are

	Ni + Ni at 1.93 AGeV	Au + Au at 1.24 AGeV
Λ production probability	$2.3 \cdot 10^{-2}$	$3.2 \cdot 10^{-2}$
signal counts	5645	2011
signal over background ratio	8.4	0.24
significance	71.0	19.8
integral efficiency · acceptance	$1.7 \cdot 10^{-3}$	$7.0 \cdot 10^{-4}$

Table 5: Results of MC simulation of 10^8 UrQMD minimum-bias events with full mCBM detector response.

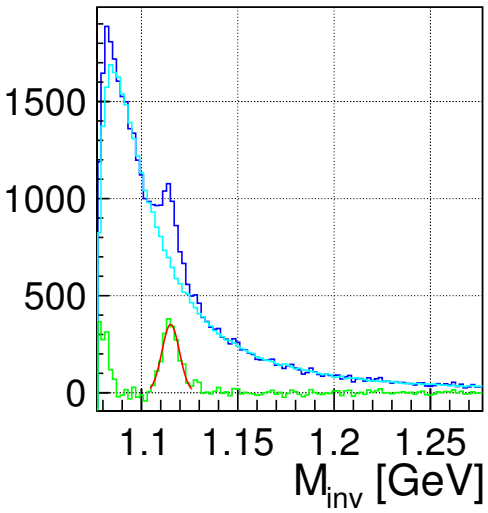

Figure 9: Λ-identification in Au + Au collisions at 1.24 AGeV. Invariant mass distributions are shown for pair combinations (combinatorics) within events (dark blue), for pair combinations from mixed events (cyan) and for the subtracted distribution (green). Statistics information is obtained from a Gaussian fit to the subtracted distribution (red line) and is summarized in Table 5.

certainly possible by tuning the selection cut values. However, at the current state of planning the presented performance obtained on a clean event based reconstruction is considered to be sufficient to demonstrate mCBM's capabilities. The real background conditions due to the streaming data taking model of CBM are not known as of today.

Thus also all the background rejection strategies necessary to reconstruct rare probes with CBM at SIS100 can be prepared and exercised with mCBM. In addition, if the technical goals of mCBM are achieved a measurement of the Λ production excitation function should become feasible. This was not yet measured in the SIS18 beam energy range thus offering a unique opportunity to contribute to world data, although the covered phase space is limited and therefore systematic errors become large when extrapolating to unmeasured regions.

The successful implementation and demonstration of the technical capabilities would also open the road to more relevant physics observables like the measurement of light hypernuclei. The beam time request for more physics oriented observables will be placed in the next beamtime period from 2020 – 2021, once the preliminary results are supporting the high expectations.

4 Installation

The installation site for the mCBM test-setup is the detector test area HTD[5] situated at the beam entrance of the experimental area Cave-C (HTC). Although the space is very limited in the HTD area, the compact mCBM setup measuring a full length of about 3 m will fit into HTD. Supply systems will have to be positioned close to side walls as well as on top of cave's concrete ceiling.

projectile	T @ 10 Tm	T @ 18.66 Tm
p	2.21 GeV	4.74 GeV
Ca	0.83 AGeV	2.02 AGeV
Ni	0.79 AGeV	1.93 AGeV
$Ag(46^+)$	0.65 AGeV	1.65 AGeV
$Au(69^+)$	0.45 AGeV	1.24 AGeV

Table 6: Kinetic energy T of various projectiles at 10 Tm and 18.66 Tm rigidity of the corresponding beam transport system.

switching magnet HTD MU1					
	radius ρ	horizontal aperture	effective deflection angle	magnetic induction B	magnetic rigidity Bρ
design track	6.25 m	110 mm	14.5°	1.6 T	10 Tm
expanded track	11.25 m	88 mm	8.0°	1.66 T	18.66 Tm

Table 7: Track parameter and resulting magnetic rigidities.

As illustrated in Fig. 10, the incoming beam will be either transported to the nuclear structure experiment R^3B or deflected to the detector test area HTD by a switching magnet (dipole magnet) mounted directly in front of Cave-C carrying the name HTD MU1[6] in the GSI nomenclature. The design of the switching magnet HTD MU1 leads for the (design) track with a bending radius of $\rho = 6.25$ m to an effective deflection angle of 14.5°, corresponding to an magnetic rigidity of B$\rho = 10$ Tm. Using HTD MU1 as currently designed would substantially limit the projectile energy available at the HTD cave. Accordingly the maximum kinetic energy T for heavy projectiles like Au would be limited to 0.45 AGeV as listed in Table 6, generating unrealistic conditions due to a large number of low-momentum fragments emitted during the collision. In order to exploit the full beam energy range of SIS18 we plan to bend the beam projectiles on the expanded track with a significantly larger bending radius ρ through the switching magnet HTD MU1. Choosing the expanded track with a radius of $\rho = 11.25$ m results for the top rigidity of the SIS18 synchrotron of 18.66 Tm in an effective deflection angle of 8.0° as given and summarized in Table 7. The design as well as the expanded track of HTD MU1 is shown in Fig. 11. The loss in horizontal aperture of 22 mm is acceptable and will not limit the beam quality.

The modification of the deflection angle into the HTD cave to 8° requires a new vacuum

[5] German abbreviation: Hochenergie Transport D

[6] German abbreviation: "MU" stands for "Magnetischer Umlenker" = "magnetic redirector"

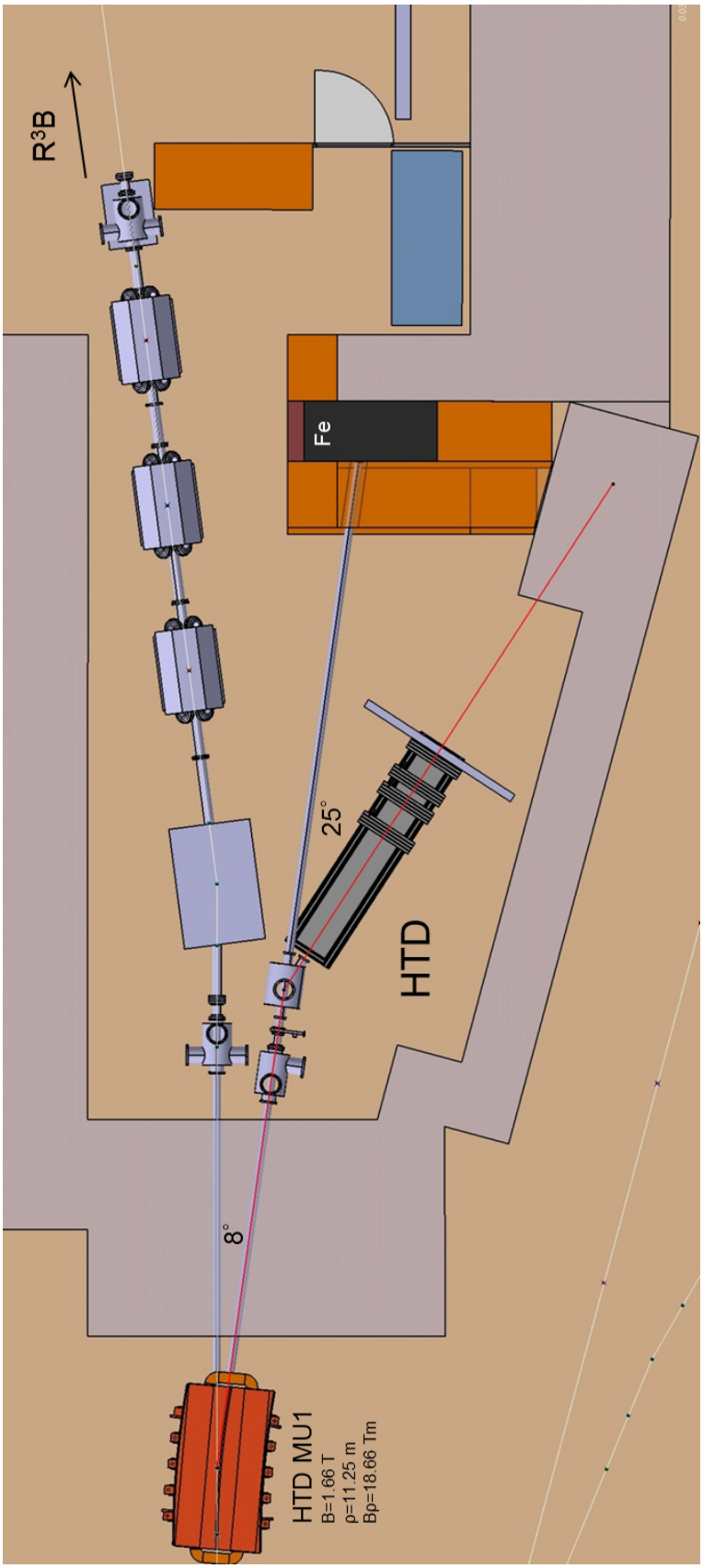

Figure 10: Design of the HTD site for the mCBM@SIS18 test-setup.

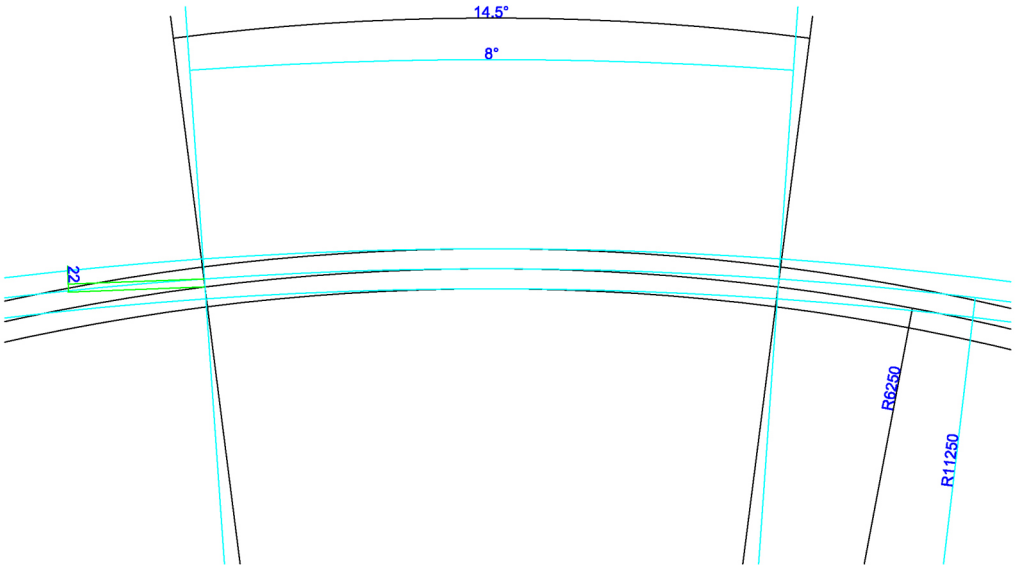

Figure 11: Radii ρ of the switching magnet HTD MU1 for the design track = 6.25 m (black) and the expanded track = 11.25 m (cyan) results in an effective deflection of 14.5° and 8.0°. The corresponding loss of horizontal aperture on the expanded track amounts to 22 mm.

chamber of the switching magnet HTD MU1. The present vacuum chamber, designed for beams under 0° and 14.5°, has to be replaced by one enabling 0° and 8.0°. Moreover, the concrete shielding wall in front of the HTD cave has to be modified to install the beam line under the new deflection angle.

The arrangement of the HTD cave for the mCBM test-setup depends substantially on the incident angle of the beam as shown in Fig. 10. This also affects shielding measures which become necessary to make high-rate beam tests feasible up to CBM design collisions rates. As one of the shielding measures, in particular for the R^3B experiment located in cave-C, a sandwich-like beam dump has been designed consisting of six 12 cm thick steel plates covered by 80 cm thick concrete blocks, considering a beam hole up to the steel core. The beam hole will be shut after irradiation. Additional concrete blocks are foreseen directly in front of the R^3B target region. To block access into the HTD cave after high-rate beam-tests have taken place, a lockable entrance door will be installed. Four additional concrete layers with a thickness of 0.8 m each will be placed on top of the HTD cave ceiling. Detailed results of the corresponding radiation level simulations using the FLUKA software package are depicted in Figs. 34 to 38 of the appendix B.2. The FLUKA simulations have been performed for Au + Au collisions at 1.24 AGeV kinetic projectile energy with a beam intensity of 10^8 ions per second and a 10% interaction target with a thickness of 2.5 mm, resulting to 10^7 interactions per second. As shown, the sandwich-like beam dump reduces the radiation intensity inside HTC as well as outside the HTD test area significantly. According to the FLUKA simulations less than 10^4 hadrons per cm^2 per second are expected around the target region of the R^3B experiment. Due to the additional shielding measures the dose rate limiting value of 0.5 μS/h can be met on top of the HTD cave ceiling.

4.1 Major milestones

Q3/2017	New vacuum chamber ($0^\circ + 8^\circ$) of the switching magnet HTD MU1 ordered
Q4/2017	New vacuum chamber of HTD MU1 mounted
Q4/2017	Beam line into the HTD cave (8°) prepared incl. concrete work
Q4/2017	Installation site HTD prepared
Q1/2018	Switching magnet HTD MU1 tested w/o beam
Q1/2018	Experiment mechanical frame and supplies mounted/installed
Q2/2018	mFLES installed and operational
Q2/2018	Detector subsystems (incl. readout) installed, tested, aligned
Q2/2018	Beam line into the HTD cave (8°) aligned and commissioned w/o beam
Q3/2018	mCBM commissioned w/o beam
Q4/2018	mCBM commissioned with beam
Q4/2019	Design performance of the free-streaming read-out system achieved
Q1/2020	Online track and event reconstruction operational
Q4/2020	1^{st} benchmark test passed
Q4/2021	2^{nd} benchmark test passed

Table 8: Major milestones of the mCBM project.

5 Application for beamtime

The beam time requests for the years 2018 and 2019 are summarized in Table 9.

2018

The time line for installation, commissioning and operation of the mCBM experiment is summarized in Table 8 of section 4.1. The setup will be commissioned in 2018 with moderate and medium interaction rates, without online data selection. For this task, we apply (1) for 30 shifts of parasitic beam time, distributed over four development weeks. At the end of that year's block of SIS18 beam we apply (2) for 21 shifts (one full week) of parasitic beam time to perform high-rate detector tests.

2019

In 2019, we intend to commission the system for highest interaction rates, with the goal to reach the design performance of the free-streaming data acquisition, time-slice building and online event reconstruction and selection by the end of the year. For that year, we again apply (3) for 30 shifts of parasitic beam in four development weeks and (4) at the end of that year's beam time block 6 shifts with Au and Ni beams as main user.

	year	objective	projectile	intensity	extraction	shift type	number of shifts
(1)	2018	developing and commissioning	ions, 1 - 2 AGeV	10^5 - 10^6 s^{-1}	slow, 10 s	para-sitic	30
(2)	2018	high-rate detector tests	ions, 1 - 2 AGeV	10^6 - 10^7 s^{-1}	slow, 10 s	para-sitic	21
(3)	2019	approaching full performance	ions, 1 - 2 AGeV	10^6 - 10^8 s^{-1}	slow, 10 s	para-sitic	30
(4)	2019	running at full performance	Au 1.24 AGeV, Ni 1.93 AGeV	10^7 - 10^8 s^{-1}	slow, 10 s	main	6

Table 9: Application for SIS18 beam time in the years 2018 and 2019 for mCBM.

Preview for 2020 and 2021

Having established the full performance, we intend to perform benchmarks physics runs in 2020 and 2021 with each year 15 shifts as main user plus 15 shifts of parasitic beam used as preparatory phase (see Table 10).

year	objective	projectile	intensity	extraction	shift type	number of shifts
2020	preparation of 1^{st} benchmark run	ions 1 - 2 AGeV, preferably: Au 1.24 AGeV, Ni 1.93 AGeV	10^7 - 10^8 s^{-1}	slow, 10 s	para-sitic	15
2020	1^{st} benchmark run, Λ reconstruction	Au 1.24 AGeV, Ni 1.93 AGeV	10^7 - 10^8 s^{-1}	slow, 10 s	main	15
2021	preparation of 2^{nd} benchmark run	ions 1 - 2 AGeV, preferably: Au 1.24 AGeV, Ni 1.93 AGeV	10^7 - 10^8 s^{-1}	slow, 10 s	para-sitic	15
2021	2^{nd} benchmark run, Λ excitation function	Au, Ni 0.8-1.93 AGeV	10^8 s^{-1}	slow, 10 s	main	15

Table 10: Preview for 2020 and 2021 of planned requirements on SIS18 beam time for mCBM.

References

[1] M. Merschmeyer et al. (FOPI collaboration),
K^0 and Λ production in Ni+Ni collisions near threshold, Phys. Rev. C 76 (2007) 024906

[2] Wojciech M. Zabołotny, Grzegorz Kasprowicz, Adrian P. Byszuk, David Emschermann, Marek Gumiński, Krzysztof T. Poźniak and Ryszard Romaniuk,
Selection of hardware platform for CBM Common Readout Interface, Proc. SPIE, vol 10445, 2017, ISBN 9781510613546

[3] J. Heuser, W. F.J. Müller, V. Pugatch, P. Senger, C. J. Schmidt, C. Sturm and U. Frankenfeld,
Technical Design Report for the CBM Silicon Tracking System (STS),
GSI-2013-05499, http://repository.gsi.de/record/54798

[4] S. Chattopadhyay, Y. P. Viyogi, P. Senger, W. F.J. Müller and C. J. Schmidt,
Technical Design Report for the CBM : Muon Chambers (MuCh),
GSI-2015-02580, https://repository.gsi.de/record/161297

[5] C. Höhne,
Technical Design Report for the CBM Ring Imaging Cherenkov Detector (RICH),
GSI-2014-00528, http://repository.gsi.de/record/65526

[6] N. Herrmann,
Technical Design Report for the CBM Time-of-Flight System (TOF),
GSI-2015-01999, https://repository.gsi.de/record/109024

[7] F. Guber and I. Selyuzhenkov,
Technical Design Report for the CBM Projectile Spectator Detector (PSD),
GSI-2015-02020, https://repository.gsi.de/record/109059

A mCBM subsystems

A.1 mSTS

Two small tracking stations, built from prototype elements of the STS detector, will be employed to provide track points close to the target in the mCBM set-up (see Fig.12).

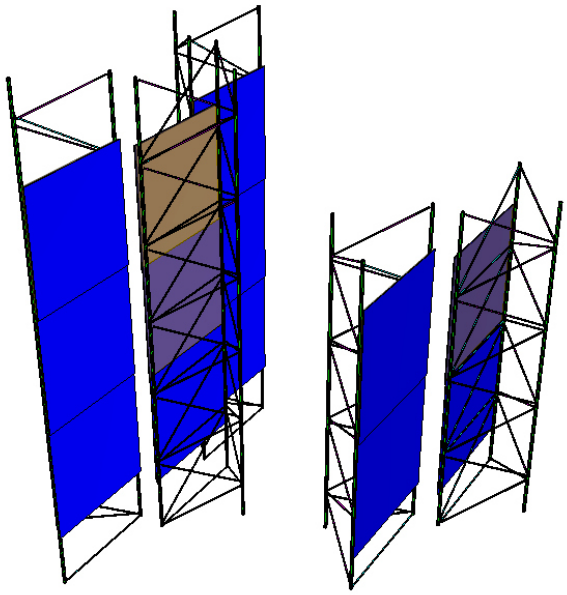

Figure 12: The present CbmRoot geometry of the mSTS subsystem.

The components are "half-ladders", i.e. detector ladders from the emerging STS construction that are cut in the middle and populated with two or three detector modules only instead of possible five. The length of the carbon fiber support structures will be shorted accordingly. The two variants of mSTS ladders are schematically shown in Fig. 13. Two of them, comprising two detector modules each, will form the first tracking station when mounted top-down onto a mechanical frame with a little lateral overlap. Three additional half-ladders, carrying three detector modules each, are to build up the second tracking station.

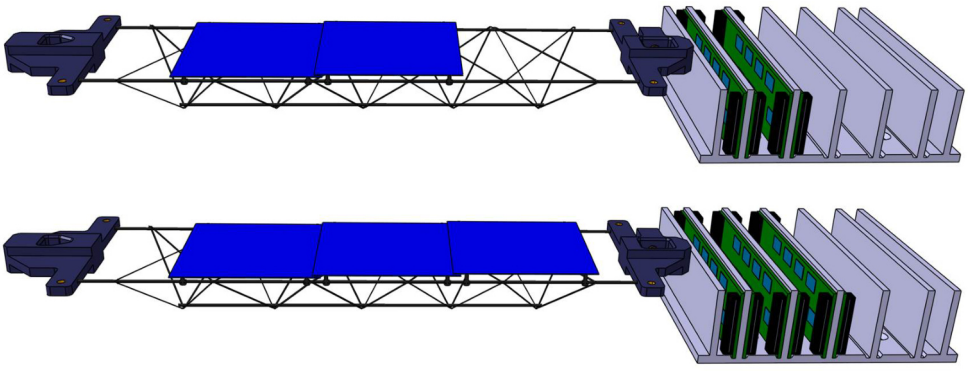

Figure 13: Schematic view of the two types of mSTS detector ladders, populated with either two (top) or three (bottom) detector modules. In the engineering drawings, only the silicon sensors mounted on the carbon fiber supports are shown, as well the front-end electronics boards installed in cooling shelves (on the right side). The interconnecting microcables have been omitted.

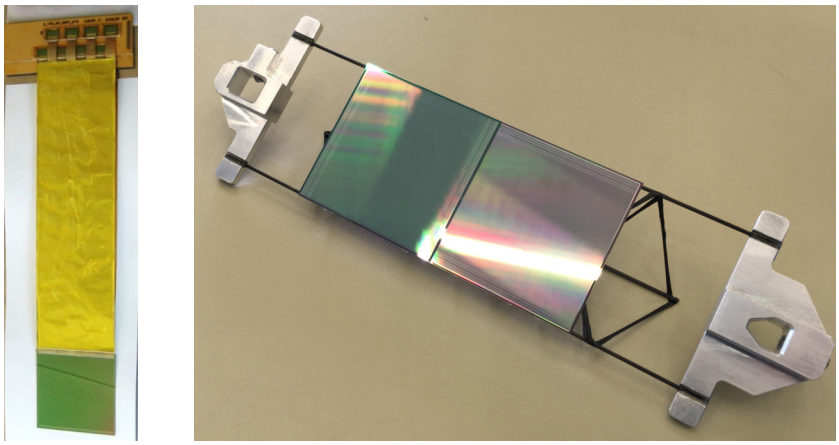

Figure 14: (left panel) Mechanical prototype of a STS detector module comprising a double-sided silicon microstrip sensor (bottom), front-end electronics (top) and a read-out microcable stack between the sensing and electronics parts. (right panel) Silicon microstrip sensors mounted on a prototype mechanical support made from carbon fiber elements and precision positioning plates.

Every module comprises a double-sided silicon microstrip sensor of 6.2 cm by 6.2 cm outer dimensions, segmented into 1024 strips per side. The strip pitch is 58 microns and the strip orientation is under 0 degrees (parallel to the ladder) and 7.5 degrees on the front and back side of the sensor. A prototype module is shown in the left panel of Fig. 14. In the right panel of the same figure, the mounting of the silicon sensors onto the carbon fiber support structure is shown — during assembly trials.

The modules with their 13 microstrip sensors present 13 x 2048 read-out strips and thus in total more than 26 thousand read-out channels, involving 208 STS-XYTER front-end ASICs. The front-end electronics boards will be attached to water-cooled plates to remove the dissipated power. Power-supply boards and further read-out electronics will be mounted in the vicinity of the stations. The two stations will be housed in a box shielding against light and electromagnetic radiation, using a low-mass beam window. Inside of the box, the sensors are operated at ambient temperature or within a cooled dry gas atmosphere.

mSTS readout

The mapping of the STS ladder front-end electronics to the readout hardware is summarized in Tab. 11, 12 and 13. The FEB-8x1 are equipped with 8 STS-XYTER ASICs and utilize 1 e-link per STS-XYTER, summing up to 8 e-links per FEB-8x1. Since each sensor has 1x n-side FEB and 1x p-side FEB, 16 e-links need to be readout for a single sensor. A ROB-3 is equipped with 3 GBTx ASICs and provides connectivity for 42 e-links. The optical connection of the ROB-3 is handled with 1 down- and 3 uplinks, occupying a total of 3 Multi-Gigabit Tranceivers (MGT) on the DPB.

In station 1 each ladder consisting of 2 sensors can be readout with a single ROB-3. However in station 2, the ladders are equipped with 3 sensors and thus would require 48 e-links, which is too much for a single ROB-3, see Tab. 11. Therefore these ladders need to be mapped differently to the ROBs. A possible solution is depicted in Tab. 12. With 9 sensors in station 2 there are 9 n-side FEBs and 9 p-side FEB. If 4 or 5 n-/p-side FEBs can be connected to a single ROB-3, then station 2 can be readout with 4 ROB-3, the entire mSTS will take 6 ROB-3. The number of DPBs required to interface these 6 ROB-3 is shown in Tab. 13. Each DPB is equipped with a FM-S18 FMC offering 8 optical ports, of which 6 ports can be used to connect GBT links, see Fig. 29. As a consequence 2 ROB-3 each using 3 MGTs can be interfaced to 1 DPB. To read out the full mSTS with 13 sensors, 6 ROB-3, 18 duplex fibers and 3 DPBs are required.

object	number of FEBs	e-links on FEBs	number of ROBs	e-links on ROBs	e-links unused
2-ladder	4	4 x 8 = 32	1	42	10
3-ladder	6	6 x 8 = 48	–	42	not enough
station 1	8	8 x 8 = 64	2	2 x 42 = 84	20
station 2	18	18 x 8 = 144	4	4 x 42 = 168	24
total	26	208	6	252	44

Table 11: Amount of FEB-8x1 and GBTx ROB-3 required to read out the mSTS.

object	e-links on FEBs	number of ROBs	e-links on ROBs	e-links unused
n-side 3+2	5 x 8 = 40	1	42	2
n-side 1+3	4 x 8 = 32	1	42	10
p-side 3+2	5 x 8 = 40	1	42	2
p-side 1+3	4 x 8 = 32	1	42	10
total	144	4	168	24

Table 12: Mapping of FEB-8x1 to GBTx ROB-3 in mSTS station 2.

object	number of ROBs	optical up-/down-links	duplex fibers	DPBs
station 1	2	2x (3+1) = 6+2	6	1
station 2 n-side	2	2x (3+1) = 6+2	6	1
station 2 p-side	2	2x (3+1) = 6+2	6	1
total	6	18+6	18	3

Table 13: Required amount of DPBs to interface the GBT links from the mSTS.

A.2 mMUCH

The sectors of the first two stations of the MUon CHamber system (MUCH) are made of trapezoidal shaped GEM modules. Three of those trapezoidal shaped GEM modules with a spacing of 10 - 20 cm will form the mMUCH subsystem (see Fig. 15, left side) providing additional tracking points for track reconstruction. While the actual CBM MUCH design comprises a spacing of about 10 cm of any two consecutive layers, a larger distance between the GEM modules for the mCBM test-setup seems to be reasonable to improve the track reconstruction. A detailed simulation in this regard may guide us towards optimum choice of these gaps.

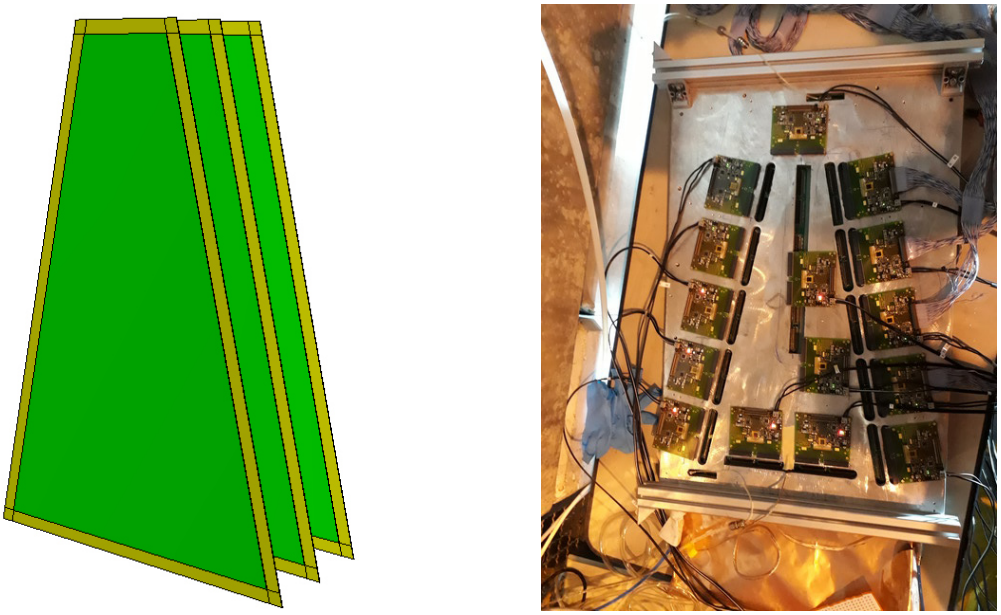

Figure 15: (left panel) - the present CbmRoot geometry of three GEM modules forming the mMUCH subsystem. (right panel) - photograph of a trapezoidal module mounted on a Aluminum plate used during the CERN-SPS test in 2016.

Each GEM module will be mounted on a 10 mm Aluminum plate as depicted in Fig. 15, right side. This photograph shows a real-size M1-type module with 15 FEBs used during the CERN SPS beam test in 2016. For mCBM the updated version M2 will be used, which is marginally larger in size. It will be read out by 18 FEBs, i.e. about 2200 channels. The detector will be positioned on one side of the Al-cooling plate, while the readout FEBs will be fixed on the other side providing a proper thermal contact to the Al-plate. A controlled water-flow either through grooved channels or through 6 mm Al-pipes winding inside the Al-plates will provide the cooling for the FEBs.

For the GEM modules single-mask triple GEM foils will be used having 24 segments each. Each of these segments will be powered by a resistive chain via an opto-coupler interface. Modules based on this approach are currently under fabrication for lab tests.

mMUCH readout

The readout of the mMUCH is summarised in Tab. 14 and 15. As for the mSTS the mMUCH will be interfaced to the DAQ employing 6 ROB-3, 18 duplex fibers and 3 DPBs.

object	number of FEBs	e-links present	number of ROBs	e-links on ROBs	e-links unused
1x M2-module	18	18 x 4 = 72	2	84	14
3x M2-module	54	216	6	252	42

Table 14: Amount of FEB-2x2 and GBTx ROB-3 required to readout the mMUCH.

object	number of ROBs	optical up-/down-links	duplex fibers	DPBs
1x M2-module	2	2x (3+1) = 6+2	6	1
3x M2-module	6	18+6	18	3

Table 15: Required amount of DPBs to interface the GBT links from the mMUCH.

A.3 mTRD

It is planned to install four TRD modules, arranged in a stack of four layers, in the mCBM setup, see Fig. 16. These modules have outer dimensions of 95 x 95 cm^2 and correspond to the large module type 8 foreseen for the final SIS100 detector. They are equipped with pad planes segmented into 6×128 = 768 rectangular pads, see Fig. 17.

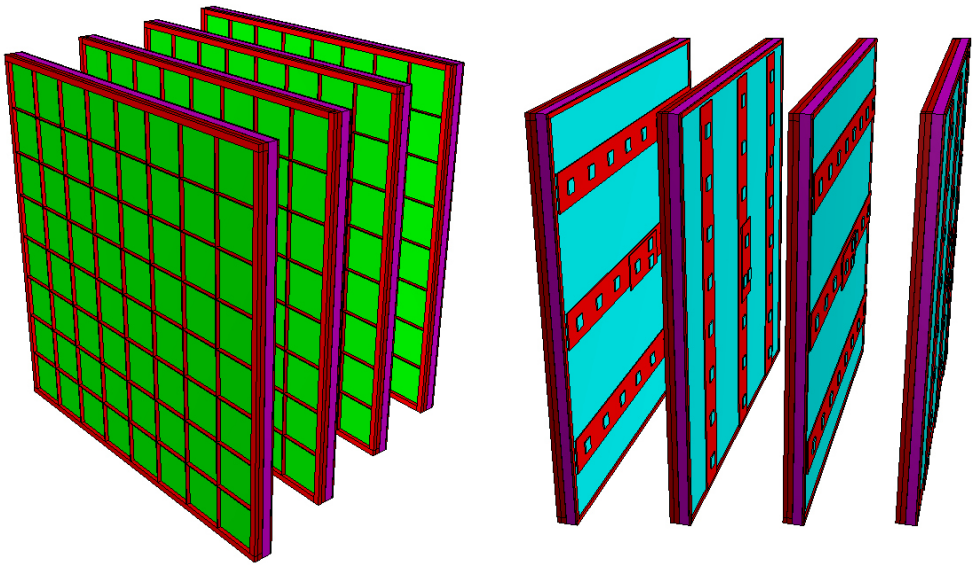

Figure 16: mTRD geometry v18e as included in the present mCBM setup in CbmRoot.

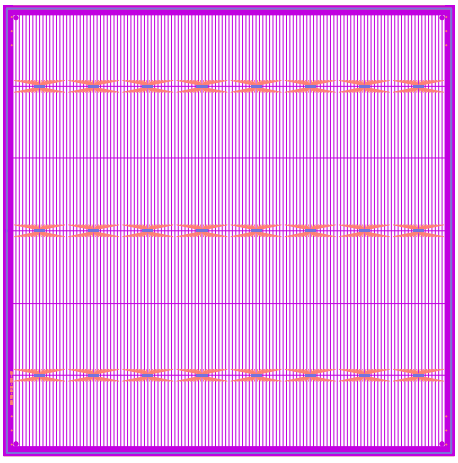

Figure 17: The pad plane layout for TRD module type 8 consists of 6 rows of 128 pads. The pads are about 7.18 mm x 150 mm in size. Each pair of pad rows will be equipped with two FEB-4x1-2. These FEBs are populated with 4 single SPADIC v2.x ASICs, each of which is interfaced with 2 e-links to the GBTx ROB.

The readout chain will employ the final version of the 32-channel SPADIC chip. Four SPADICs will be arranged per Front-End Board (FEB), such that overall 24 FEB-4x1-2 will be needed to equip all 4 TRD modules. These FEBs are currently being designed and should be available on time for operation in mCBM. Data will be transferred from the FEB through ROBs via GBT links to the DPB layer, thus following the same readout scheme as for the final experiment at SIS100.

The four readout chambers foreseen for mCBM were already constructed, together with their support structure. During a test beam campaign at the CERN-SPS in November 2016 (see Fig. 18) they were tested and successfully operated over a longer period of time. During these tests, however, only few channels were read out. For operation in mCBM they will have to be fully instrumented with the final readout electronics. Also, a prototype gas system has been constructed, which can be used for the mTRD in mCBM.

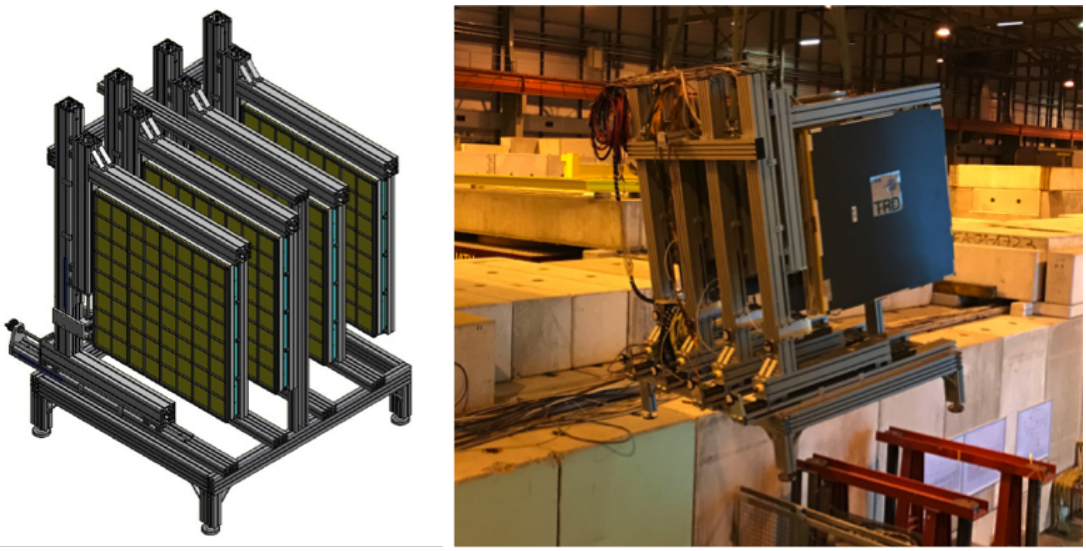

Figure 18: (left) 3D model of the mTRD subsystem. (right) Photograph of the mTRD subsystem taken during installation at the CERN SPS beam test in November 2016.

mTRD readout

The TRD uses the GBTx ROB-3 as interface to the data acquisition system. Each SPADIC is connected via 2 e-links to the GBTx ASICs. These TRD modules will finally be equipped with 24 SPADICs per module requiring 48 e-links. As a consequence each TRD module will be fitted with 2 ROB-3, see Tab. 16. To read out the mTRD with 24 FEB-4x1-2, the chain will consist of 8 ROB-3, 24 duplex fibers and 4 DPBs, as derived in Tab. 17.

object	number of FEBs	e-links on FEBs	number of ROBs	e-links on ROBs	e-links unused
module type 8	6	6 x 8 = 48	2	84	36
total	24	192	8	336	144

Table 16: Amount of FEB-4x1-2 and GBTx ROB-3 required to read out the mTRD.

object	number of ROBs	optical up-/down-links	duplex fibers	DPBs
module type 8	2	2x (3+1) = 6+2	6	1
total	8	24+8	24	4

Table 17: Required amount of DPBs to interface the GBT links from the mTRD.

A.4 mTOF

The TOF group contributes with the mTOF subsystem consisting of five full size modules from type M4 (see Fig. 19) including the complete front-end electronic chain (PADI FEE, Get4 FEE, GBTx ROB) and infrastructure.

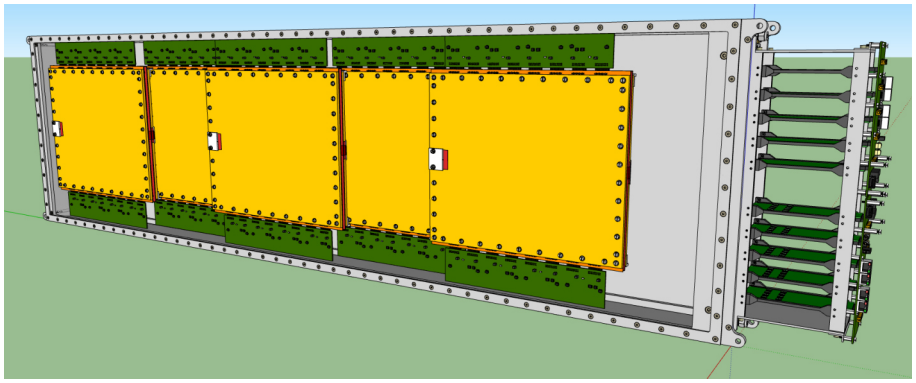

Figure 19: Technical drawing of a mTOF M4 module, holding 5 MRPC3a counters.

Each module comprises 5x MRPCs from type MRPC3a [1], 10x PADI FEE preamplifier/discriminator boards (32 channels each), 10x Get4 FEE TDCs (32 channels each), and 2x Readout Boards equipped with a single GBTx chip. The MRPC3a counter has 32x readout strips with a pitch of 1 cm and a strip length of 27 cm. The strips are read out on both sides.

The counters containing low resistive glass show a rate capability higher than 20 kHz/cm^2 and are foreseen for the intermediate rate region of the CBM TOF system. The total active area of the mTOF is 150 x 125 cm^2 and comprises 1600 read out channels. The infrastructure for the system consists of a clock distribution, a LV power supply (TDK Lambda) with 8 V and 90 A, a 6 kV HV power supply (CAEN or ISEG) with 5 negative and 5 positive channels and an open loop gas system. The present CbmRoot geometry of the mTOF subsystem is depicted in Fig. 20.

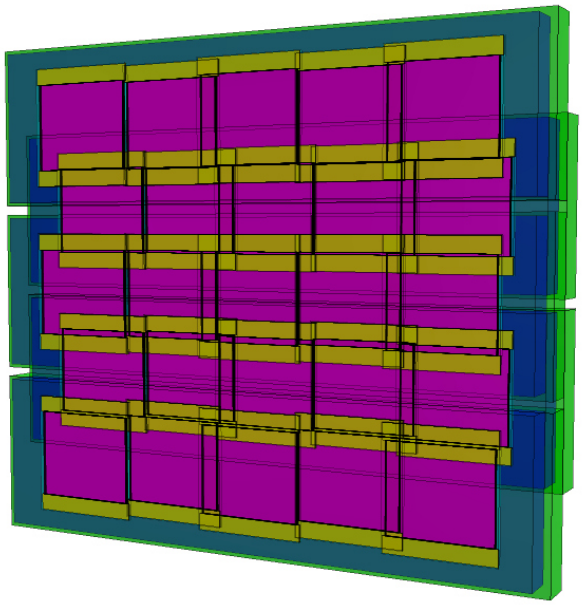

Figure 20: The CbmRoot geometry of the mTOF v18e subsystem.

A.4.1 T_0 counter

For the Time-of-Flight (TOF) based particle ID the reference timing is going to be provided by the dedicated T_0 counter. The design goal for the time resolution of T_0 is 50 ps (including readout chain) based on the overall TOF resolution of 80 ps. The detector is necessary in the calibration/test phase of the TOF wall, while in high multiplicity events a software determination of T_0 will be carried out.

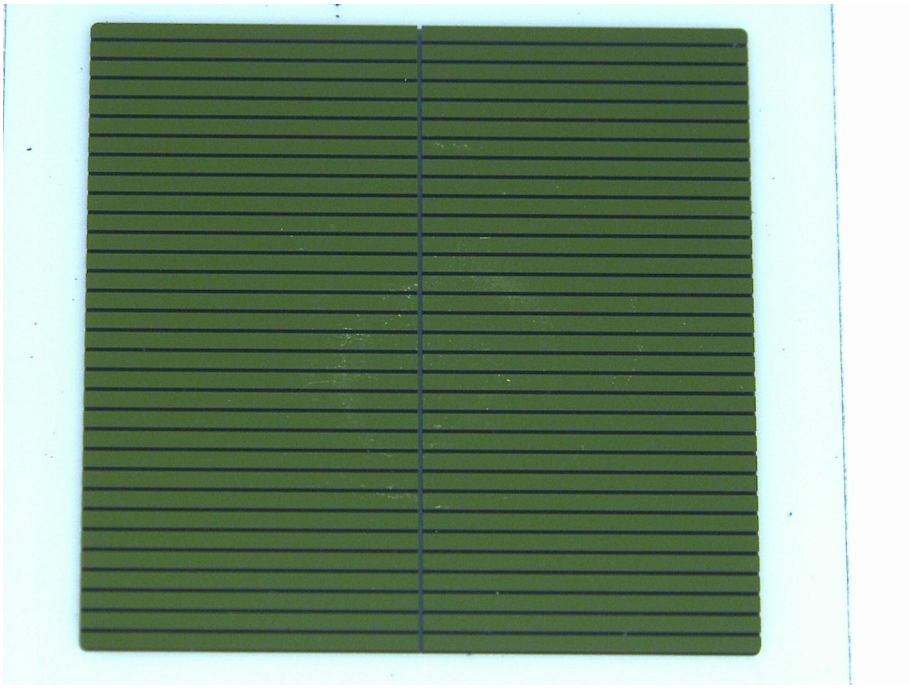

Figure 21: The multi-segmented diamond plate of the T_0 counter.

The in-beam T_0 detector for the measurements with heavy-ion beams in the mCBM setup is going to be constructed from an electronic grade polycrystalline diamond plate of 0.3 mm thickness (s. Fig. 21). A single plate of 20 mm x 20 mm is going to be placed in a beam-pipe vacuum upstream from the target. The segmentation of the readout electrodes comprises two goals; monitoring of the beam quality and position (detector is mounted in stationary position relative to the optical beam axis) and that the peak data load on each channel can be processed by the readout electronics (digitizer). The first stage of the analogue front-end electronics is integrated on the PCB together with detector and high-voltage bias. The amplified signals are carried over a multi-pin vacuum feed-through connector to the outer part of the front-end electronics, where additional signal amplification, shaping and discrimination are taking place. The timing signals are processed with same kind of digitizers as TOF signals and they are synchronized to the same reference clock. At high rates, the data overhead needs to be suppressed in conjunction with the data processing from the TOF wall. While the common clock guarantees the synchronization between both subsystems, the data throttling is independent, which can lead to unnecessary data loss.

The prototype of the actual device is being constructed by the HADES collaboration and is going to be used in a production run in 2018.

mTOF readout

In contrast to the mSTS, mMUCH and mTRD subsystems, which use 3 GBTx ASCIs on a single ROB-3 board, the mTOF will build a ROB-1 with a single GBTx ASIC. The total number of GBT up- and downlinks is therefore symmetrically distributed for mTOF. Its readout system will consist of 10 ROB-1, interfaced with 10 duplex fibers to 2 DPBs, as listed in Tab. 18.

object	number of ROBs	optical up-/down-links	duplex fibers	DPBs
1x M4 module	2	2x (1+1) = 2+2	2	1
total	10	10+10	10	2

Table 18: Required amount of DPBs to interface the GBT links from the mTOF.

A.5 mRICH

The prototype of the Ring Imaging CHerenkov detector (RICH) to be used in mCBM will use a glass, quartz or aerogel radiator in proximity focusing operation mode. It will be placed behind the mTOF detector in a selected acceptance window and deliver a second measurement of the velocity of the particles. In combination with mTOF it should be possible to separate at least protons and kaons and thus improve the PID and thus momentum measurement in mCBM.

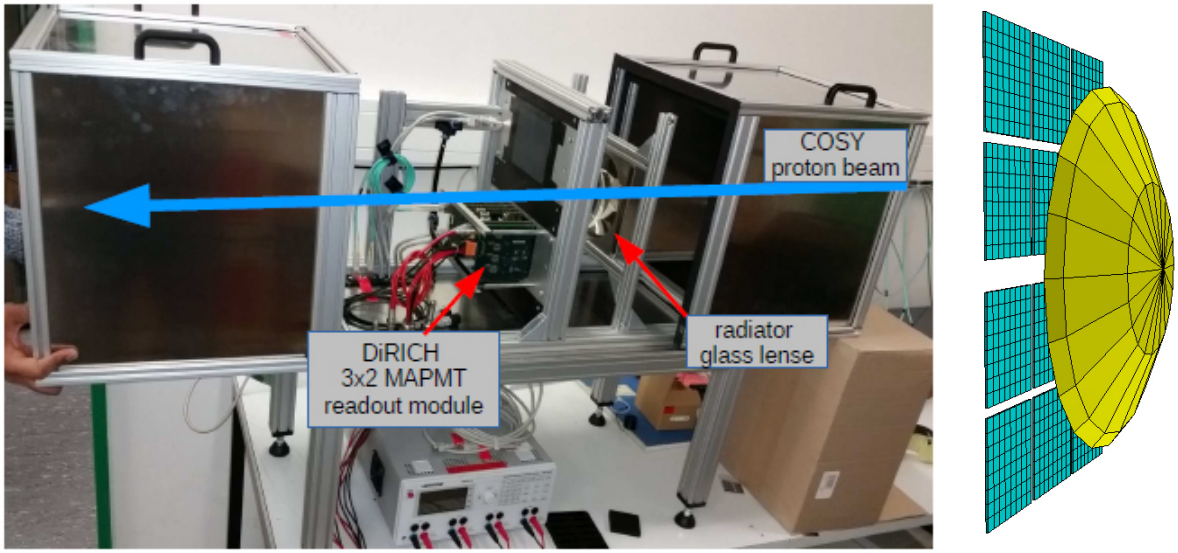

Figure 22: (left panel) Photograph of the COSY prototype testbox, with radiator lense in the right compartment, and a single 6x MAPMT DiRICH backplane with power-, combiner- and few DiRICH front-end modules mounted in the left compartment. The beam will pass from right to left. (right panel) Geometry model of the small RICH prototype in CbmRoot, consisting of the radiator lense (yellow) and the 2 groups of 2x3 MAPMTs (cyan), representing 2 DiRICH modules.

The mRICH prototype to be used will be an extended version of a RICH prototype built for detector tests with the proton beam from COSY (see Fig.22). This mRICH would be operated with either a glass lense of 15 cm diameter or a quartz or glass plate of 10x10 cm^2. As MAPMT array two 2x3 MAPMT modules will be employed covering an area of about 350 cm^2. The radiator to be chosen will be determined in detailed simulations and depends on the momentum distribution of the produced particles and the achievable ring characteristics. This basic concept can easily be extended to an array of 2x2 glass lenses or larger plates thus covering a larger acceptance. The mRICH setup will be added to mCBM in 2019. Before, the CBM RICH group will finish the HADES RICH upgrade in cooperation with HADES and bring the detector into operation in the first HADES beamtime at SIS18 in 2018. By then, the electronics will be mature and fully integrated in the TRBnet readout of HADES.

In order to integrate the TRBnet based RICH readout into the general CBM DAQ scheme, a dedicated module on the DPB/CRI board will receive TRBnet based data messages, build corresponding micro-slices out of these data, and insert them into the CBM data stream. Development and qualification of this TRBnet CBM datalink, and in particular the synchronization between TRBnet based readout and CBM DAQ is one of the main motivations for mRICH.

A.6 mPSD

A supermodule of the CBM Projectile Spectator Detector (PSD) consisting of an array of 3 x 3 = 9 individual PSD modules (mPSD, see Fig. 23) will be used at the mCBM test-setup for determination of the collision geometry. The mPSD subsystem measures 60 x 60 cm^2 in transverse dimensions, 165 cm in length and weights approximately 5 t. For beam intensities larger than 10^6 ions per second, the central module will be removed.

Figure 23: Assembled mPSD supermodule near the test beam line at CERN.

In 2017 and 2018 the response of the PSD modules will be studied at the CERN T10 and T9 test beam lines at the PS using hadron beam momenta of $2 - 10$ GeV/c. The supermodule will be read out by Dubna front-end electronics with 64Ms ADCs, PADIWA AMPS and Time-Over-Threshold based electronics (TRB3).

In the second half of 2018 the supermodule will be delivered to GSI/FAIR for installation and integration into the mCBM test-setup. The final PSD readout electronics type will be chosen after the PSD supermodule tests to include the mPSD into the CBM DAQ system in 2019.

A.7 mECAL

The CBM ECAL subsystem (see Fig.24) consists of in total 1088 "shashlik" like modules segmented

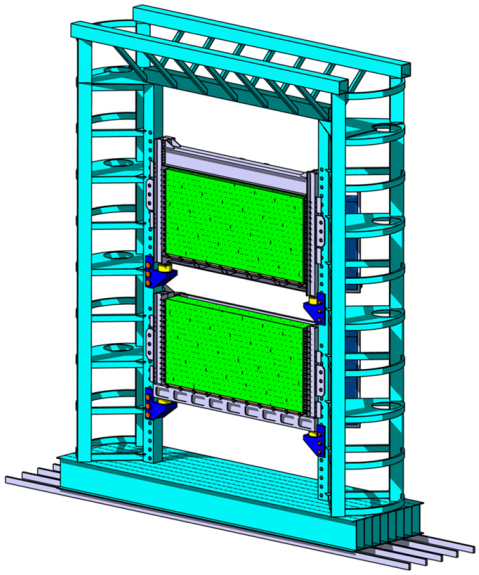

Figure 24: Design of the (complete) CBM ECAL subsystem.

into four cells (see Fig.25). Each module covers an active area of 6 x 6 cm^2. For the mCBM setup a small calorimeter will be assembled, consisting of 25-49 modules in a 5 x 5 or 7 x 7 matrix. The readout chain for the CBM ECAL subsystem has to be developed and will be tested and optimized during the mCBM phase.

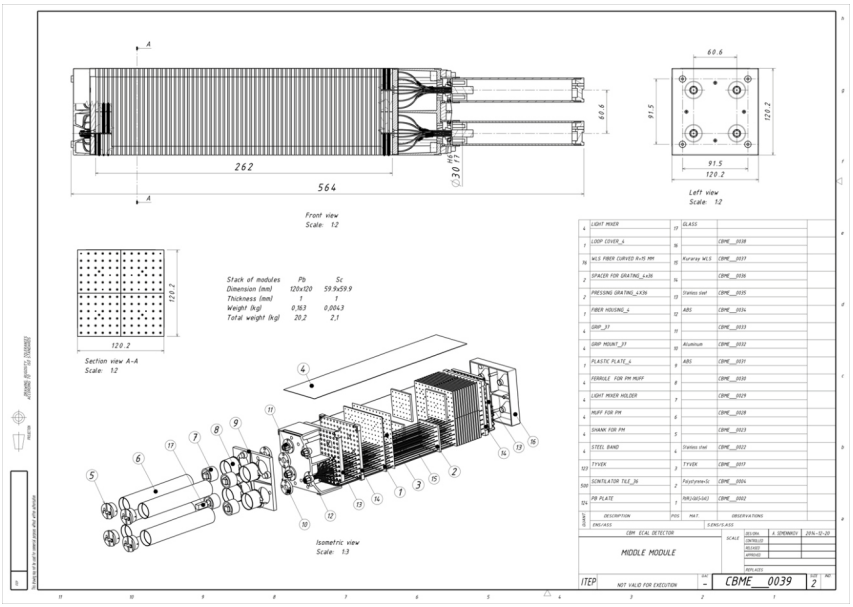

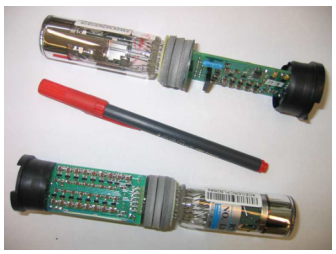

Figure 25: Design drawing of a CBM ECAL module (left) and photograph of a PMT (right).

A.8 mMVD

A one or two-plane mMVD assembly will complement mCBM once the CBM pixel sensor MIMOSIS becomes available and has been qualified in dedicated sensor test campaigns. The other prerequisite will be the GBTx based sensor readout being developed in parallel to the MIMOSIS submissions. According to the current MIMOSIS road map, the first full size MIMOSIS generation becomes available for integration in 2019, the third one in 2021. Hence, MVD may contribute to the anticipated second phase of mCBM starting in 2020.

A.9 mDAQ and mFLES

As already mentioned in the introduction to the readout section, the mCBM DAQ system will be deployed in two phases. During the start-up of mCBM (phase I) in 2018, already available readout chains based on existing prototype implementations of DPB and FLIB will be employed, see Fig. 26. The readout will focus only on the GBTx-based subsystems (mSTS, mMUCH, mTRD and mTOF), see Tab. 19. An upgrade of the readout chain will mark the transition to phase II, due 2019. During this upgrade, the FLES input nodes will be moved from the Green IT Cube to the DAQ container. A Common Readout Interface (CRI), which will be a PCIe Gen 3 x16 board, will be mounted in the FLES input nodes. The CRI will replace the DPB and FLIB boards and combine their functionality in a single FPGA, see Fig. 27. This prototype board will take up to 12 GBT links as input and interface them to the FLES input node memory. This CRI-based readout chain will be the first prototype implementation for the CBM experiment at SIS100.

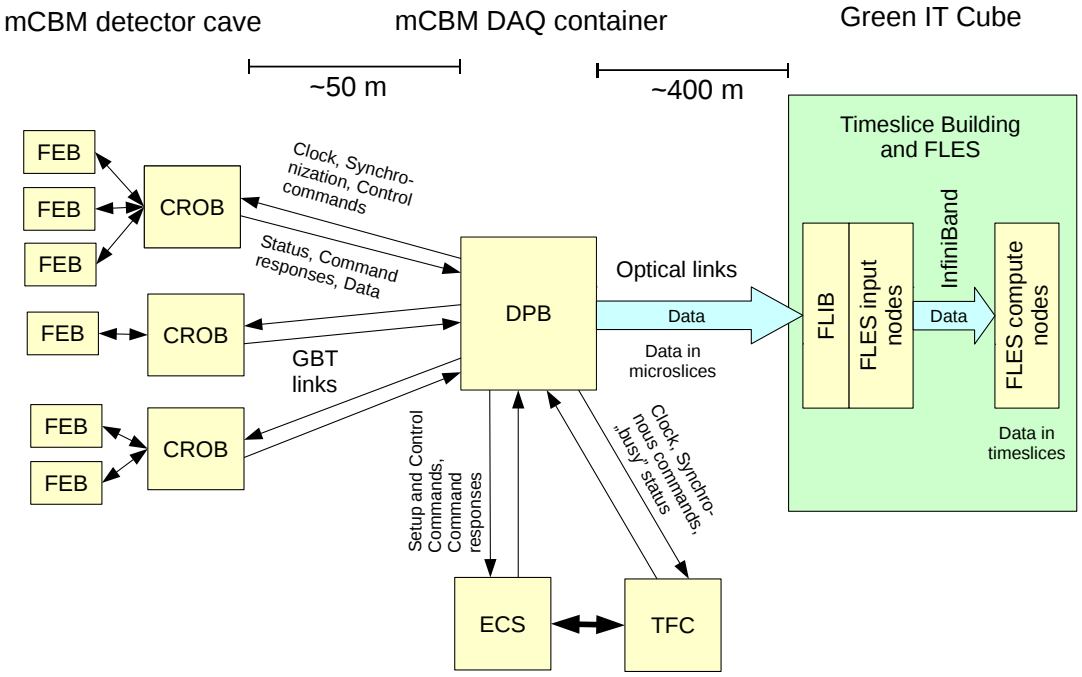

Figure 26: Proposed mCBM readout chain for phase I, based on existing DPB and FLIB prototypes, adapted from [2]. The data is sent in micro-slices from the DPBs via single-mode optical fibers to the FLES input nodes located in the Green IT Cube. The micro-slices are then forwarded via InfiniBand network to the FLES compute nodes, where the micro-slices are processed to time-slices. The time-slices are finally used in the online analysis.

In phase I (see Fig. 26), the GBT links are forwarded to the Data Processing Boards (DPB), which are currently realized as AFCK boards operated in a MicroTCA crate, see Fig. 5. Preprocessing of the data, e. g. time sorting of the input streams (mSTS) or feature extraction (mTRD), can be performed at this stage. The amount of DPBs required during phase-I of mCBM is summarized in Tab. 19. The DPBs partition the data streams into micro-slices and merge several slower (4.48 Gbit/s) GBT links into a single 10 Gbit/s high-speed link. This link will be realised with a bunch of single mode optical fibers installed between the DAQ container in the target hall and the Green IT Cube. This single mode fiber ends at the FLIB board located inside the FLES input node. The current FLIB prototype is a Kintex-7 based PCIe Gen2 x8 board

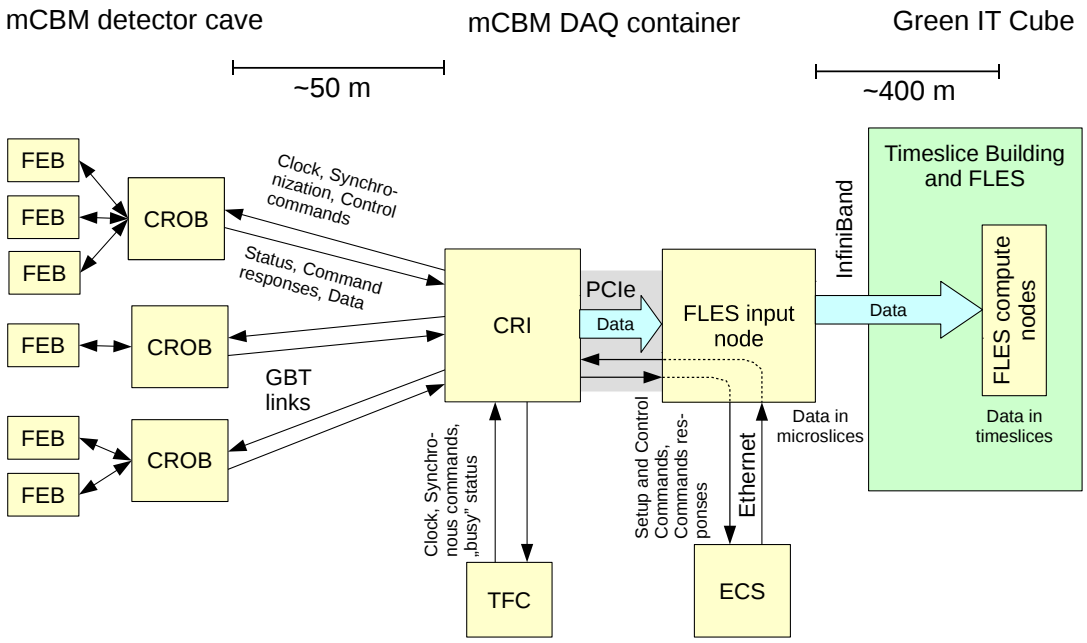

Figure 27: Proposed mCBM readout chain for phase II, based on a CRI prototype board, adapted from [2]. The CRI board is a PCIe card operated in the FLES input nodes, which were moved from the Green IT Cube into the DAQ container close to the mCBM experimental setup. The connection to the FLES computing nodes installed in the Green IT Cube is done with long-range EDR InfiniBand equipment. The stream of micro-slices sent from the FLES input nodes is combined to time-slices in the FLES compute nodes.

subsystem	ROB-1	ROB-3	GBTx	AFCK
mSTS		6x	18x	3x
mMUCH		6x	18x	3x
mTRD		8x	24x	4x
mTOF	10x		10x	2x
total	10x	20x	70x	12x

Table 19: Amount of GBT links and AFCKs used in the readout system during phase I, under the assumption that each AFCK can take 6 GBT links and without matching the bandwidth of the GBT links to the FLIB bandwidth to PCIe. The numbers are input from the respective subsystem readout summaries in Tab. 13, 15, 17 and 18.

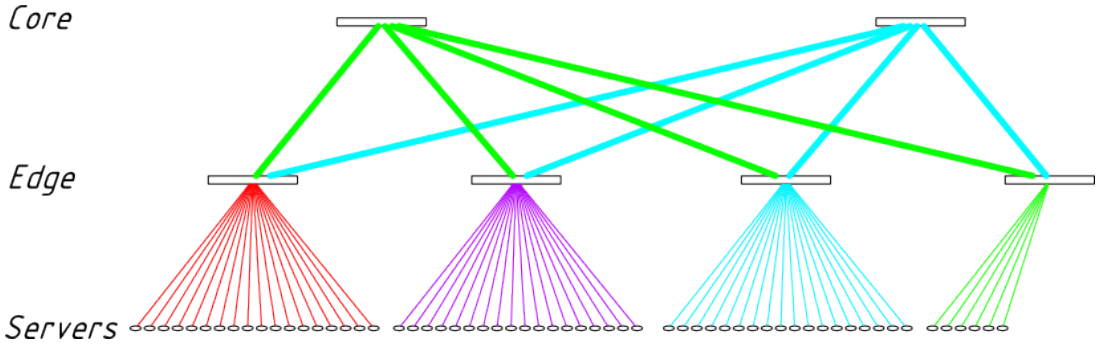

Figure 28: Possible fat-free network topology to be used for the InfiniBand network cabling of the FLES, from *www.clusterdesign.org*. Both FLES input nodes (IN) and FLES compute nodes (CN) will be connected to edge switches. The fat-tree topology allows to interface any IN with any CN at full bandwidth, which allows to build time-slices from micro-slices concurrently and on the fly.

(HTG-K700), which can receive up to either 4 or 8 optical FLIM links from the AFCKs. The data arriving at the FLIB is indexed and forwarded to its FLES input node, which transmits the data via an InfiniBand network to the FLES compute cluster located in the Green IT Cube. A dedicated topology (Fat-Tree, see Fig.28) of the InfiniBand network in the Green IT Cube allows to receive micro-slices originating from all active mCBM subsystems in a single FLES compute node. This FLES compute node combines all those micro-slices into a single time-slice, which is then passed to the reconstruction and analysis stage.

In 2019, with phase II, the mCBM readout scheme will be transformed into a prototype of the CBM@SIS100 DAQ chain. The FLES input nodes will be transferred from the Green IT Cube into the DAQ container, located in vicinity to the mCBM cave. Here DPB and FLIB prototypes (see Figs. 29 and 30), which are two separate FPGA boards, will both be replaced by the CRI (see Fig. 31) a PCIe card with a single UltraScale+ FPGA [2]. The planned CRI will be mounted in the FLES input node and will be capable of handling up to 12 GBT links. The GBTx modules on the detector front-ends will then directly connect to the CRI, dropping the MicroTCA layer. The CRI combines in one board the DPB functionality with the micro-slice handling and PCIe interface of the FLIB. Major blocks of the DPB and FLIB firmware will be re-used in the CRI FPGA design. Now that the FLES input node is located in the DAQ container, it needs to be attached to the distant InfiniBand network in the Green IT Cube to allow for time-slice building on the FLES compute nodes. This long range InfiniBand connection will be realized using the same single mode optical fiber infrastructure as used for the DPB to FLIB connection in phase I.

In addition to the upgrade of the CRI, the mCBM subsystems (mRICH, mPSD) readout with FPGA TDCs chains will also be added to the DAQ setup in 2019.

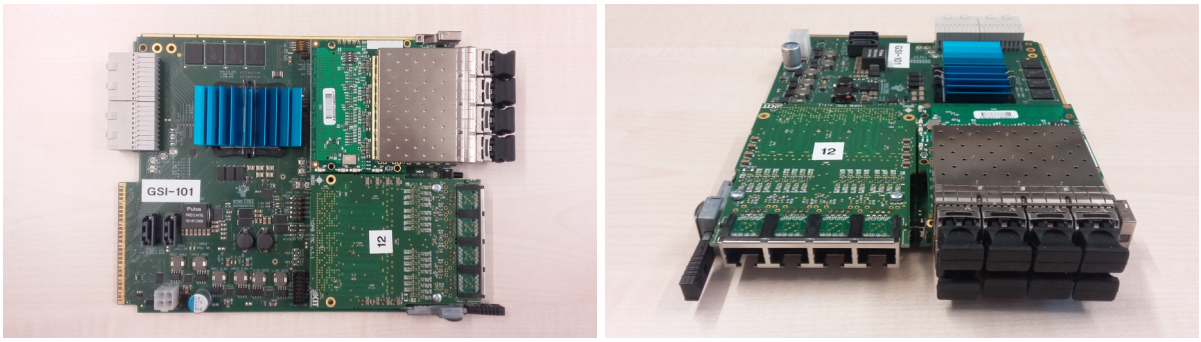

Figure 29: AMC FMC Carrier Kintex (AFCK) board, a Xilinx Kintex-7 FPGA board in AMC form factor equipped with a FM-S18 FMC and a tDPB FMC. An AFCK with this configuration can be used to interface 6x incoming GBT links at 4.48 Gbit/s to 1x outgoing FLIM link.

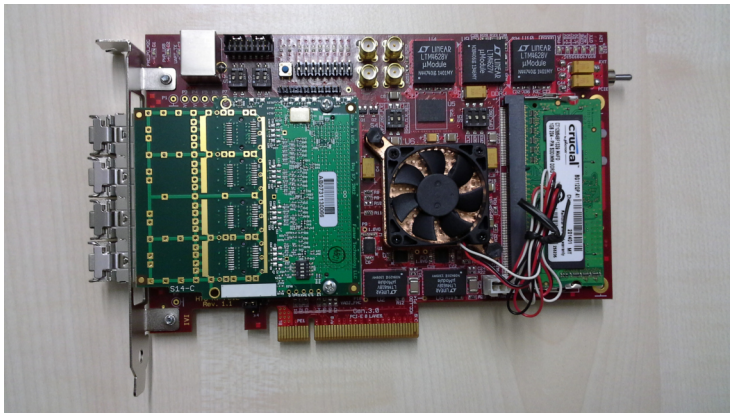

Figure 30: FLES Interface Board (FLIB), a Xilinx Kintex-7 FPGA board with PCIe Gen2 x8 interface equipped with a FM-S14 FMC, offering 4x 10 Gbit/s links. The FLIB is the current interface into the FLES Input Node (as of June 2017).

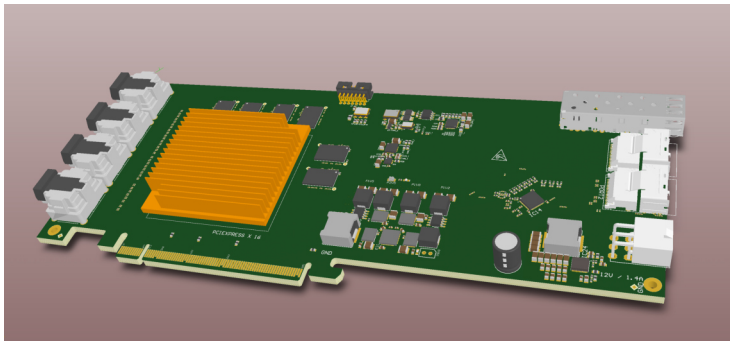

Figure 31: Draft of a Common Readout Interface (CRI) board [2] as a PCIe Gen3 x16 device interfacing 24 GBT links. The CRI will be the main component of the DAQ upgrade in 2019, replacing both DPB and FLIB.

A.10 Detector Control System mDCS

The Detector Control System for mCBM (mDCS) will be based on the EPICS (Experimental Physics and Industrial Control System) which provides an architecture for building scalable distributed control systems. Each sub detector group will provide EPICS based individual Input Output Controllers (IOC) to access on one side the hardware sensors and actors to be controlled and monitored connected via field buses or LAN. On the other side those EPICS IOCs serve their obtained data, their process variables to the local network. Optionally, if available a common platform, FTLMC, could be used for radiation loaded areas, otherwise standard PCs or mini-PCs will be used. EPICS Clients connected to this network will visualize, archive, monitor those process variables. It is foreseen to mainly use the CS-Studio framework for those tasks. As an example for this the 3 tier HADES RICH DCS hierarchy is shown in Fig. 32.

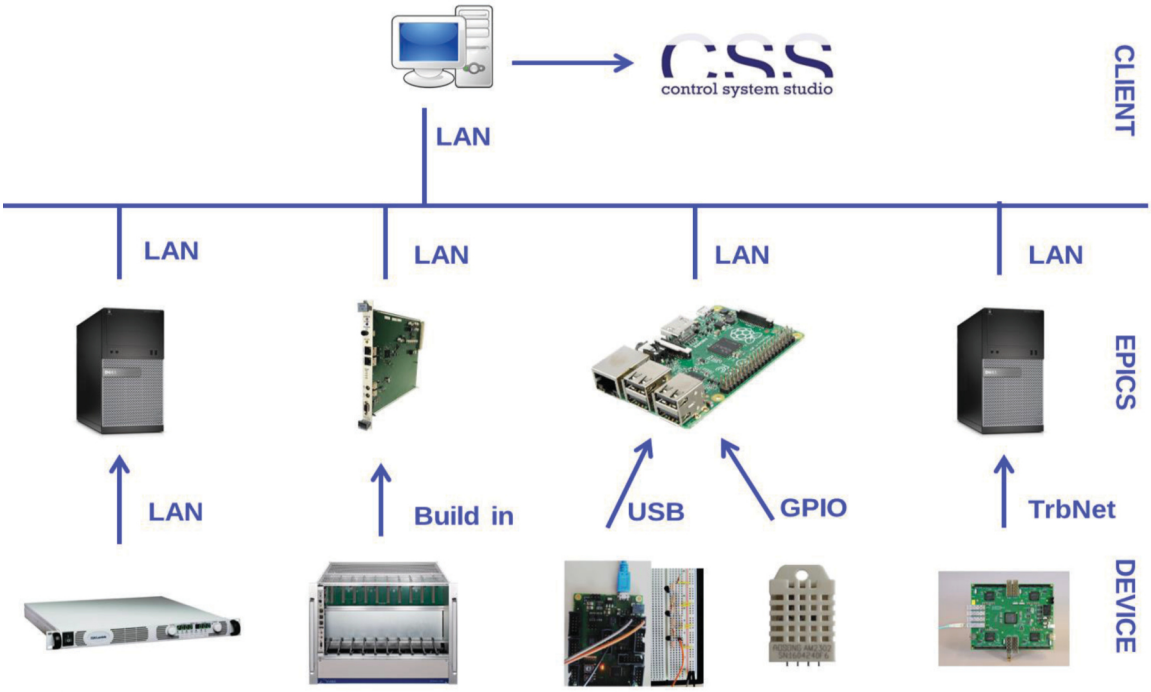

Figure 32: An example for the application of the CS-Studio framework – the 3 tier HADES RICH DCS hierarchy.

While the individual detectors provide the hardware access and infrastructure, the overall SCADA features including trending, archiving, and alarming can be centrally provided. As an option an additional separation level could be implemented to operate each detector in their own local networks, which themselves are accessed via gateways to filter data flow, control access and tune process loads. Only data needed for higher controls would then be provided via those gateways.

B mCBM installation

B.1 HTD cave layout

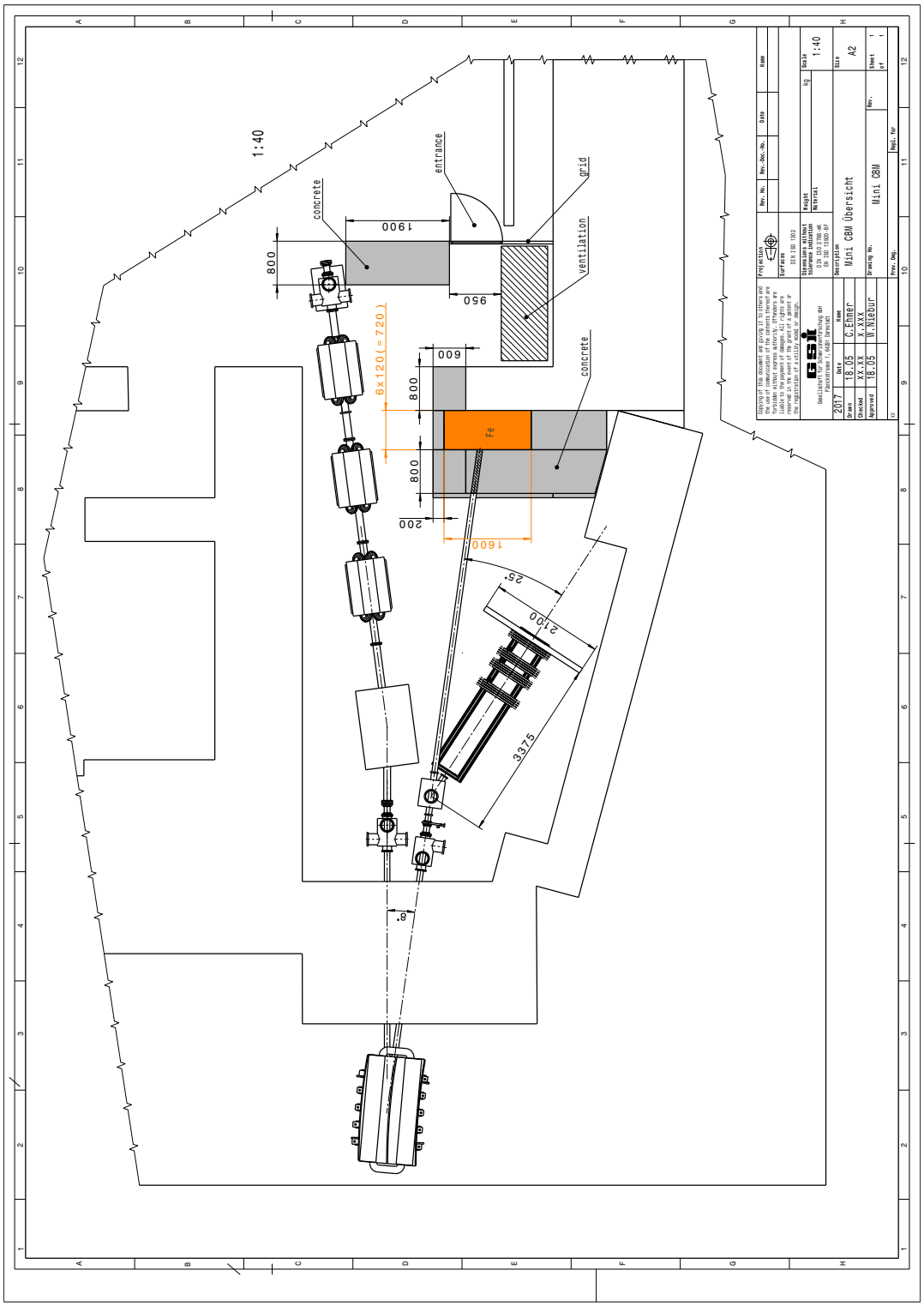

Figure 33: Design drawing of the HTD site for the mCBM test-setup.

B.2 Radiation safety

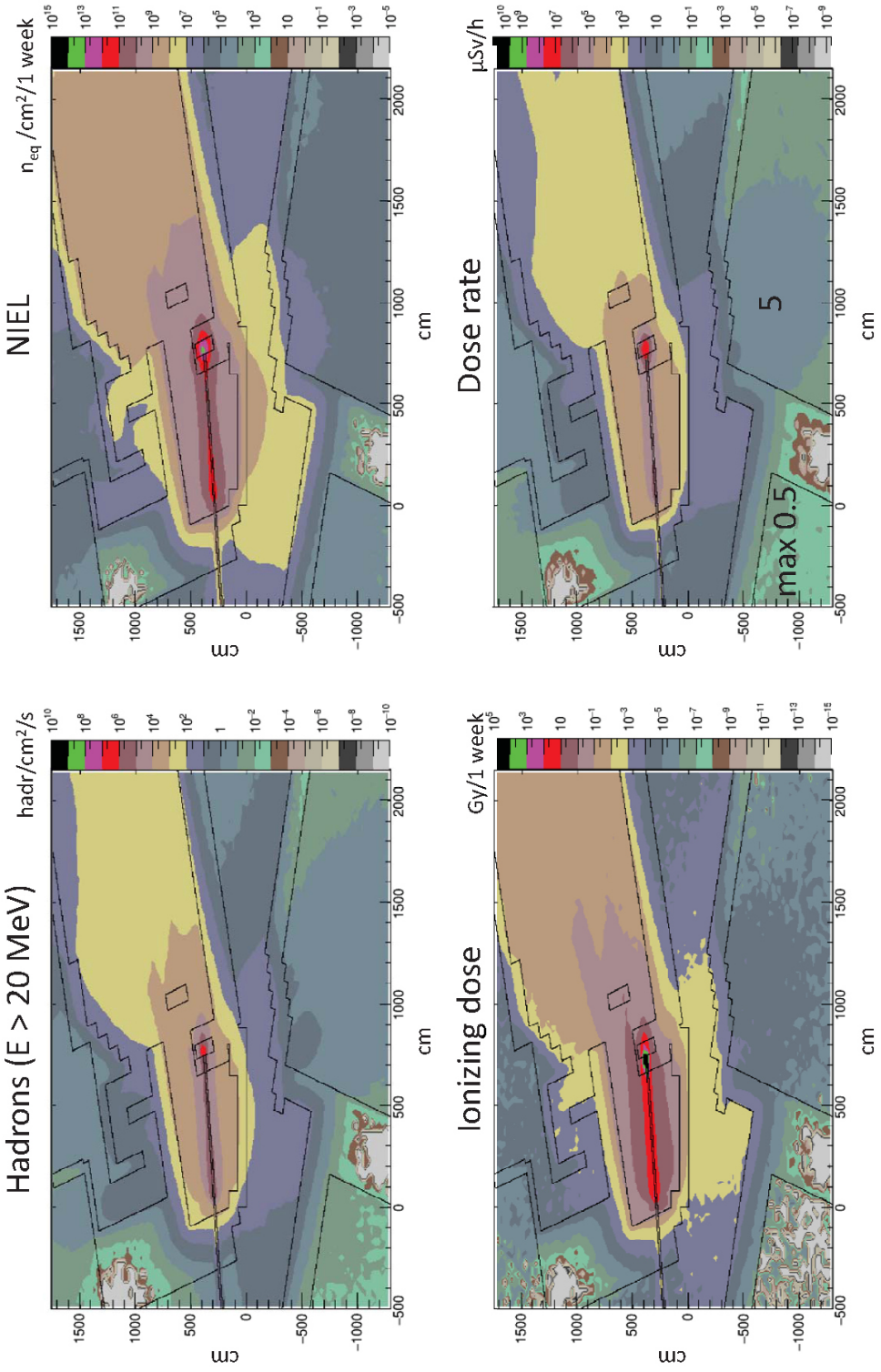

Figure 34: FLUKA simulation of the radiation field inside the HTD and HTC cave as well as neighboring areas. Beam: 10^8 Au ions per second, kinetic projectile energy: 1.24 AGeV, target: 2.5 mm Au (10 MHz interaction rate).

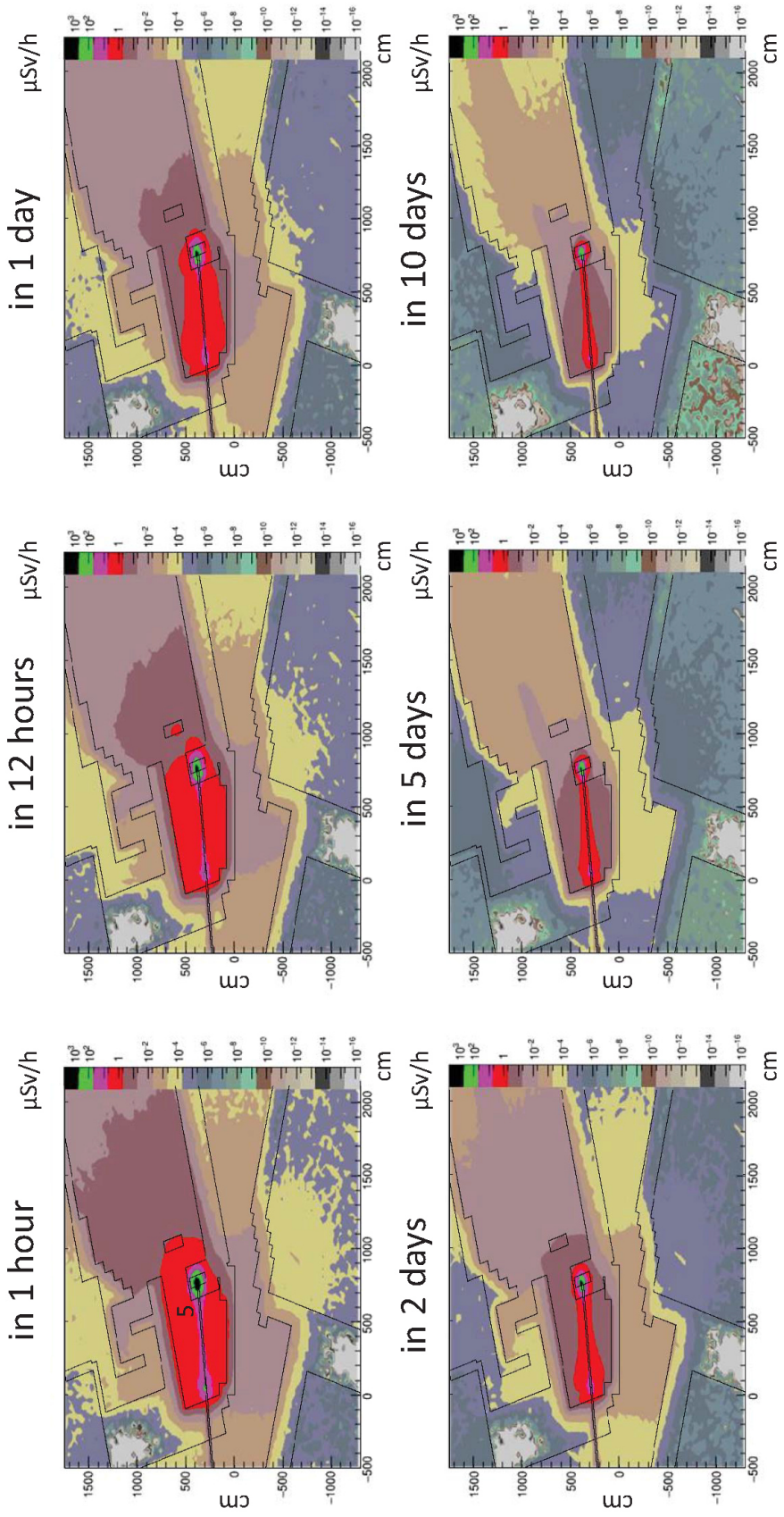

Figure 35: FLUKA simulation of the dose rate due to activation after one week of irradiation inside the HTD and HTC cave as well as neighboring areas. Beam: 10^8 Au ions per second, kinetic projectile energy: 1.24 AGeV, target: 2.5 mm Au (10 MHz interaction rate).

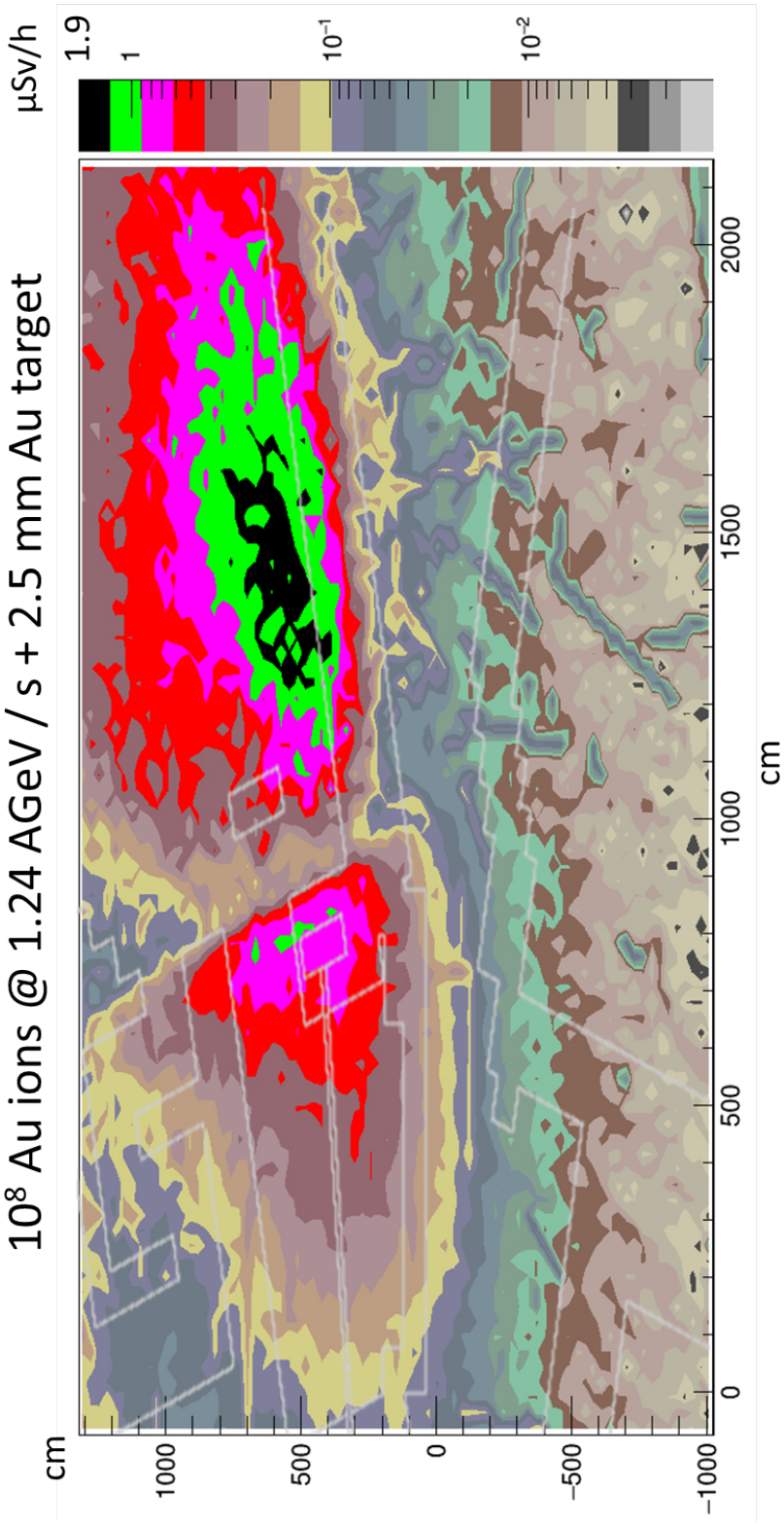

Figure 36: FLUKA radiation simulation of the dose rate on the HTD and HTC ceiling bombarding 10^8 Au ions per second with a kinetic energy of 1.24 AGeV on a 2.5 mm Au target ($\rightarrow$ 10 MHz interaction rate). Three additional concrete layers of 0.8 m thickness each have been added on top of the present HTD ceiling (within the FLUKA geometry). Despite the enhanced shielding the top dose rate on the HTD ceiling of 1.2 μS/h as well as of 1.9 μS/h on the HTC ceiling still exceed the limiting value of 0.5 μS/h. Further measures become necessary - see Fig. 37.

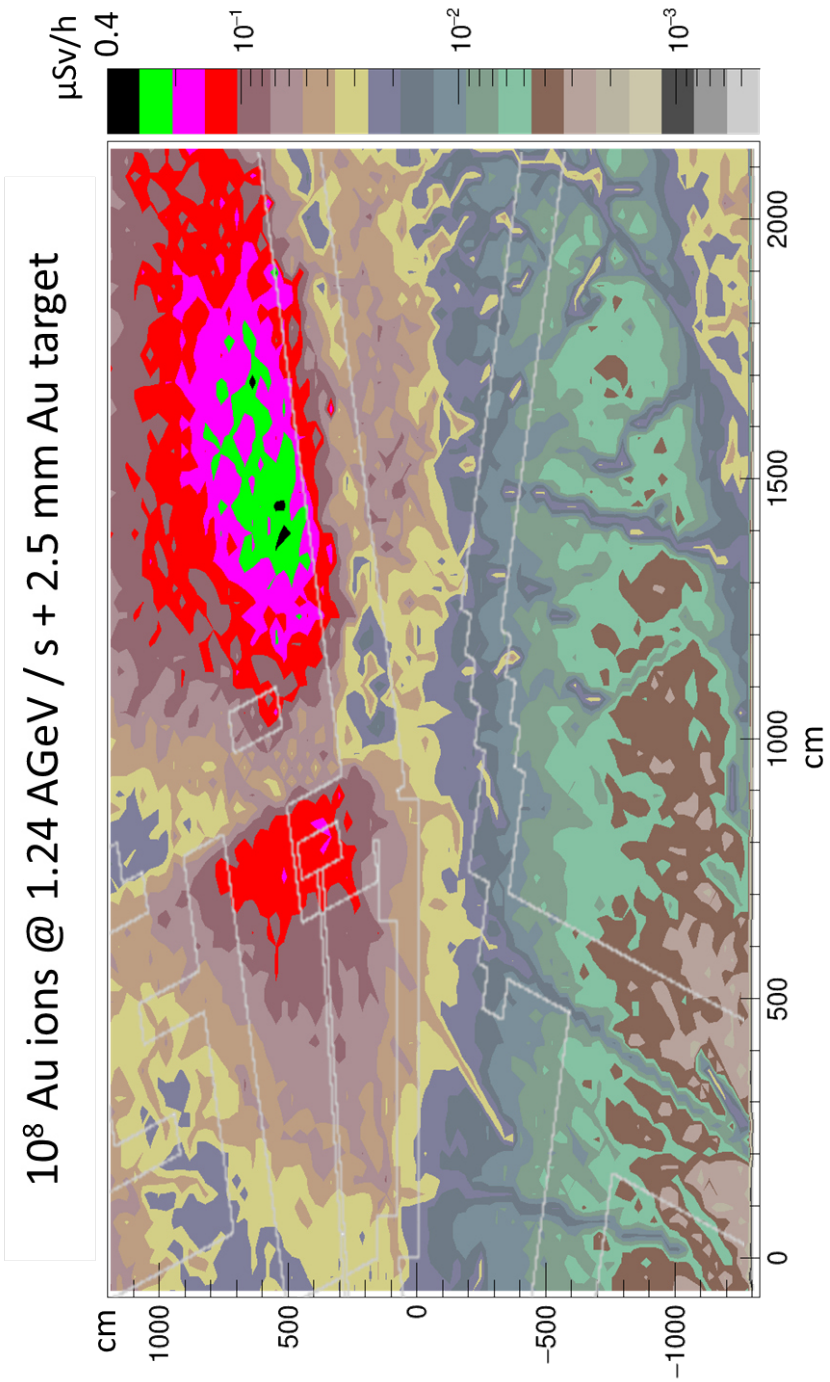

Figure 37: FLUKA radiation simulation of the dose rate on the HTD and HTC ceiling bombarding 10^8 Au ions per second with a kinetic energy of 1.24 AGeV on a 2.5 mm Au target ($\rightarrow$ 10 MHz interaction rate). To further reduce the dose rate on the HTD and HTC ceiling (see Fig. 36) another layer concrete blocks (0.8 m thickness) has been added on top of the HTD and HTC ceiling (within the FLUKA geometry) decreasing the top dose rates to 0.2 μS/h (HTD) and 0.4 μS/h (HTC) which fulfills the limiting value. Currently, the technical feasibility to add a concrete layer to the HTC ceiling can not be guaranteed. However, there is also room for improvement to adapt the beam dump design for this purpose. Furthermore, it could be considered to restrict the access to the HTD and HTC ceiling area during the few days of mCBM experiments at the highest beam intensities.

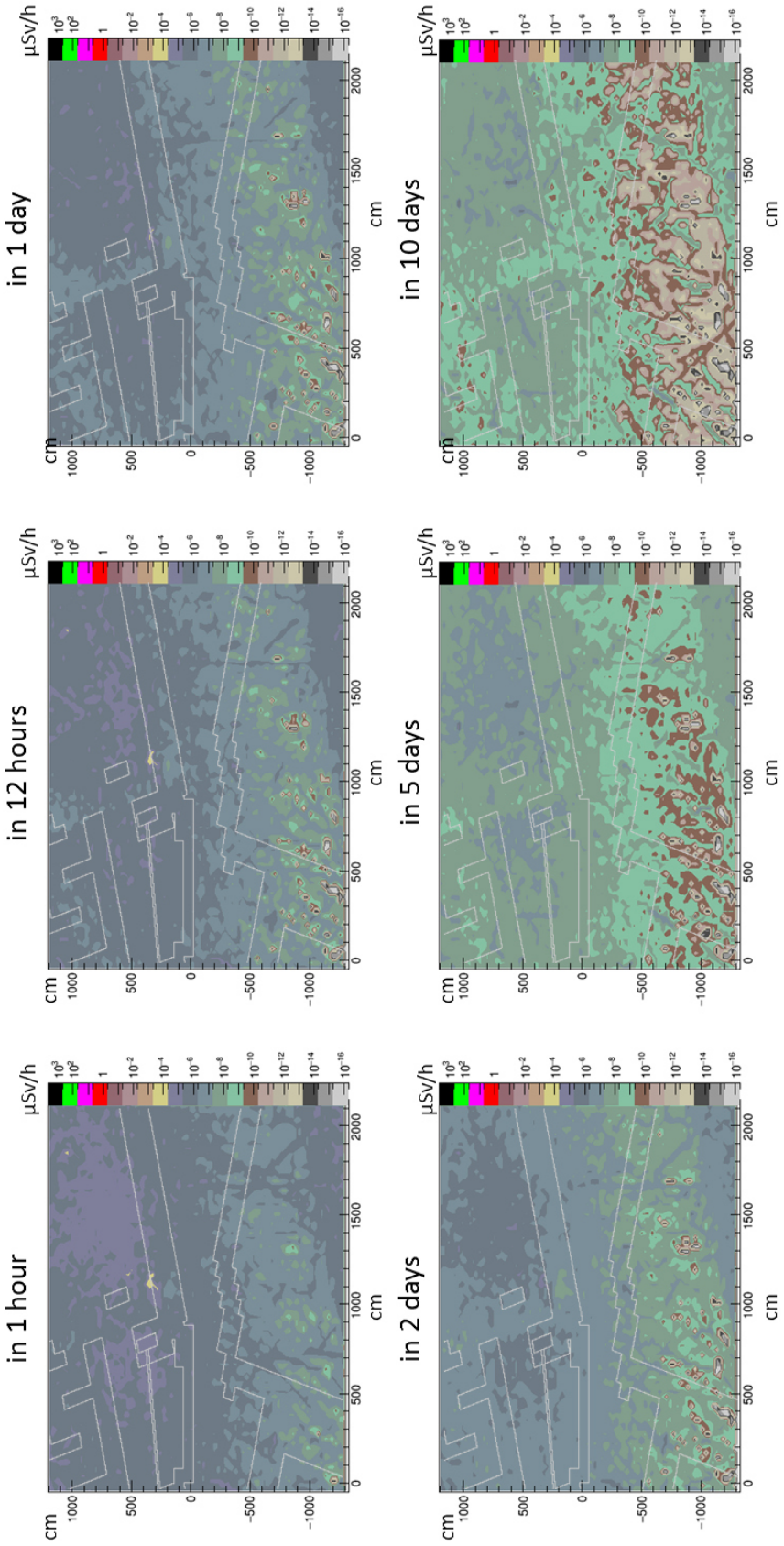

Figure 38: FLUKA simulation of the dose rate due to activation after one week of irradiation on top of the HTD cave ceiling after enhancing the shielding by four additional concrete layers of 0.8 m thickness each and a single additional layer on top of the HTC cave ceiling. Beam: 10^8 Au ions per second, kinetic projectile energy: 1.24 AGeV, target: 2.5 mm Au (10 MHz interaction rate).

C List of Acronyms

A:	ADC	Analog-to-Digital Converter
	AFCK	AMC FMC Carrier Kintex
	AGS	Alternating Gradient Synchrotron
	ALICE	A Large Ion Collider Experiment
	AMC	Advanced Mezzanine Card
	ANN	Artificial Neural Network
	ASIC	Application Specific Integrated Circuit
	AWRF	Anode Wire Response Function
B:	BDT	Boosted Decision Tree
	BNL	Brookhaven National Laboratory
	BR	Branching Ratio
C:	CBM	Compressed Baryonic Matter
	CERN	Conseil Européen pour la Recherche Nucléaire
	CF	Carbon Fibre
	CFRP	Carbon Fibre Reinforced Plastic
	CLK	CLocK
	CPU	Central Processing Unit
	CRI	Common Readout Interface
	CSA	Charge Sensitive Amplifier
D:	DAQ	Data AcQuisition
	DCS	Detector Control System
	DPB	Data Processing Board
	DSP	Digital Signal Processor
	DSTRD	Double-Sided TRD
	DTW	Drift Time Window
E:	ECAL	Electromagnetic CALorimeter
	ECS	Experiment Control System
	ENC	Equivalent Noise Charge
	ENOB	Effective Number Of Bits
F:	FAIR	Facility of Antiproton and Ion Research
	FASP	Fast Analog Signal Processor
	FEB	Front-End Boards
	FEE	Front-End Electronic
	FIFO	First In First Out
	FLES	First Level Event Selector
	FLIB	FLES Interface Board
	FLIM	FLES Interface Module

	FMC	FPGA Mezzanine Card
	FNR	First Neighbor Readout
	FPGA	Field Programmable Gate Array
	FT	Flat Top
	FWHM	Full Width Half Maximum
G:	GBT	GigaBit Transceiver
	GEANT	GEometry ANd Tracking
	GEM	Gas Electron Multiplier
	GH	Glueing Hours
H:	HDMI	High-Definition Multimedia Interface
	HDL	Hardware Description Language
	HSD	Hadron String Dynamics
	HT	High Tension
	HV	High Voltage
I:	ID	IDentification
	IIR	Infinite Impulse Response
	IMR	Intermediate Mass Region
	ISO	International Organization for Standardization
J:	JINR	Joint Institute of Nuclear Research
L:	LFR	Likelihood Function Ratio
	LHC	Large Hadron Collider
	LQ	Likelihood derived from charge (Q) measurement
	LS	Layer Support
	LV	Low Voltage
M:	MADC	Multiplexed Analog-to-Digital Converter
	MAPD	Multi-Avalanche Photo-Diodes
	MAPS	Monolithic Active Pixel Sensors
	MAPT	Multi-Anode Photomultiplier Tubes
	MBS	Multi Branch System
	MC	Monte Carlo
	MIP	Minimum Ionizing Particle
	MPO	Multi-fiber Push On connector
	MPV	Most Probable Value
	MRPC	Multi-gap Resistive Plate Chambers
	MSV	Modularized Start Version
	MUCH	MUon CHambers
	MVD	Micro Vertex Detector
	MWPC	Multi-Wire Proportional Chamber

N:	NICA	Nuclotron-based Ion Collider fAcility
	NIEL	Non-Ionizing Energy Loss
	NIST	National Institute of Standards and Technology
P:	PASA	Pre-Amplifier Shaping Amplifier
	PC	Power Consumption
	PCB	Printed Circuit Board
	PDF	Probability Density Function
	PE	PolyEthylene
	PID	Particle IDentification
	PMMA	PolyMethylMethAcrylate
	POB	POwer Boards
	PP	PolyPropylene
	PRF	Pad Response Function
	PS	Power Supply
		Proton Synchrotron
	PSD	Participant Spectator Detector
	PWR	PoWeR (USB socket)
Q:	QDC	Charge-to-Digital Converter
	QGP	Quark-Gluon Plasma
R:	RCT	Readout ConTroler
	REQ	REQuest signal
	RHIC	Relativistic Heavy-Ion Collider
	RICH	Ring Imaging CHerenkov
	RPC	Resistive Plate Chamber
	RST	ReSeT signal
	ROB	Read-Out Board
	ROC	Read-Out Chamber
S:	SIS	Schwer-Ionen Synchrotron
	SPADIC	Self-triggered Pulse Amplification and Digitization ASIC
	SPS	Super Proton Synchrotron
	SSTRD	Single-Sided TRD
	ST	Shaping Time
	STAR	Solenoidal Tracker At RHIC
	STS	Silicon Tracking System
T:	TFC	Timing and Flow Control system
	THR	THReshold
	TOF	Time-Of-Flight
	TR	Transition Radiation

	TRD	Transition Radiation Detector
	TTL	Transistor-Transistor Logic
U:	UDP	User Datagram Protocol
	UrQMD	Ultra-relativistic Quantum Molecular Dynamics
	UMC	United Microelectronics Corporation
	UV	Ultra-Violet
V:	VTR	Versatile TransReceiver
	VTT	Versatile Twin-Transmitter
W:	WH	Working Hours
	WHPD	Working Hour Per Day
	WHPW	Working Hour Per Week
	WLS	WaveLength Shifter
X:	XT	Cross-Talk
	XYTER	X-Y-Time-Energy Readout

D The CBM Collaboration

T. Ablyazimov[1,2], R.P. Adak[3], M. Adamczyk[4], K. Agarwal[5], M.M. Aggarwal[6], Z. Ahammed[7], F. Ahmad[8], N. Ahmad[9], S. Ahmad[8], A. Akindinov[10], P. Akishin[1], V. Akishina[11,1,2], M. Al-Turany[2], I. Alekseev[10], E. Alexandrov[1], I. Alexandrov[1], C. Andrei[12], A. Andronic[2], Yu. Anisimov[13], H. Appelshäuser[11], E. Atkin[14], R. Averbeck[2], M.D. Azmi[9], S. Bähr[15], M. Balzer[15], N. Baranova[16], D. Bartoş[12], S. Bashir[8], M. Baszczyk[17], M. Baznat[13], J. Becker[15], K.-H. Becker[18], J. Beckhoff[19], S. Belogurov[1,14], A. Belousov[20], J. Bendarouach[21,2], I. Berceanu[12], A. Bercuci[12], R. Berendes[19], C. Bergmann[19], D. Bertini[2], O. Bertini[2], G. Bertolone[22], O. Bezshyyko[23], P.P. Bhaduri[7], A. Bhasin[24], A.K. Bhati[6], B. Bhattacharjee[25], A. Bhattacharyya[26], T.K. Bhattacharyya[27], S. Biswas[3], T. Blank[15], D. Blau[28,14], C. Blume[11], J. Brzychczyk[4], T. Bus[11], A. Bychkov[13], A. Byszuk[29], M. Călin[30], Ping Cao[31], G. Caragheorgheopol[12], V. Cătănescu[12], A. Chakrabarti[26], S. Chattopadhyay[7,3], A. Chaus[32], Jianping Cheng[33], H. Cherif[11,2], M.I. Ciobanu[2,55], G. Claus[22], F. Constantin[12], M. Csanád[34], Supriya Das[3], Susovan Das[5], J. de Cuveland[20], B. Debnath[25], D. Dementiev[13], Wendi Deng[35], Zhi Deng[33], H. Deppe[2], I. Deppner[36], O. Derenovskaya[1], C.A. Deveaux[21], M. Deveaux[11], K. Dey[25], Sheng Dong[35], A. Dorokhov[22], P. Dorosz[17], G. Dozière[22], J. Dreyer[37], A.K. Dubey[7], M. Dürr[21], V.V. Elsha[13], D. Emschermann[2], H. Engel[38], J. Eschke[39,2], Xingming Fan[37,56], O. Fateev[13], Sheng-Qin Feng[40], F. Fidorra[19], S.P.D. Figuli[15], P. Fischer[41], H. Flemming[2], J. Förtsch[18], P. Foka[2], U. Frankenfeld[2], V. Friese[2], E. Friske[5], I. Fröhlich[11], J. Frühauf[2], J. Gajda[17], T. Galatyuk[42,2], G. Gangopadhyay[26], C. García Chávez[38],J. Gebelein[38], C. Ghosh[7], P. Ghosh[39], S.K. Ghosh[3], S. Gläßel[11], M. Goffe[22], L. Golinka-Bezshyyko[23], S. Golovnya[43], M. Golubeva[44], D. Golubkov[10], A. Gómez Ramírez[38],S. Gorbunov[20], S. Gorokhov[43], D. Gottschalk[36], P. Gryboś[17], F. Guber[44], K. Gudima[13], M. Gumiński[29], A. Gupta[24], Yu. Gusakov[13], Dong Han[33], H. Hartmann[20], Shu He[35], J. Hehner[2], N. Heine[19], A. Herghelegiu[12], N. Herrmann[36], J.M. Heuser[2], A. Himmi[22], C. Höhne[21], R. Holzmann[2], Dongdong Hu[31], C. Hu-Guo[22], Guangming Huang[35], Xinjie Huang[33], Xiru Huang[31], D. Hutter[20], A. Ierusalimov[13], M. Irfan[9], D. Ivanischev[45], M. Ivanov[2], P. Ivanov[14], Victor Ivanov[1,14], Vladimir Ivanov[45,14], A. Ivashkin[44], H. Jahan[9], T. Janson[38], A. Jipa[30], I. Kadenko[23], P. Kähler[19], B. Kämpfer[37,56], K.-H. Kampert[18], R. Karabowicz[2], N. Kargin[14], D. Karmanov[16], K. Kasiński[17], G. Kasprowicz[29], M. Kaur[6], A. Kazantsev[28], U. Kebschull[38], G. Kekelidze[13], M.M. Khan[9], A. Khanzadeev[45,14], F. Khasanov[10], A. Kiryakov[43], M. Kiš[2], I. Kisel[20], P. Kisel[11,2,1], S. Kiselev[10], T. Kiss[46], P. Klaus[11], R. Kłeczek[17], Ch. Klein-Bösing[19], V. Klochkov[2,11], P. Kmon[17], K. Koch[2], L. Kochenda[45,14], P. Koczoń[2], M. Kohn[19], B. Komkov[45], M. Korolev[16], I. Korolko[10], R. Kotte[37], A. Kovalchuk[32], M. Koziel[11], G. Kozlov[20,1], V. Kozlov[45], V. Kramarenko[13], P. Kravtsov[45,14], E. Krebs[11], I. Kres[18], D. Kresan[2], M. Krieger[41], A.V. Kryanev[1,14], E. Kryshen[45], A. Krzyżanowska[17], M. Kuc[47], W. Kucewicz[17], L. Kudin[45], A. Kugler[48], A. Kumar[7], L. Kumar[6], A. Kurepin[44], N. Kurepin[44], P. Kurilkin[13], V. Kushpil[48], S. Kuznetsov[13], V. Kyva[32], V. Ladygin[13], C. Lara[38], P. Larionov[11,2], A. Laso García[37], E. Lavrik[5], I. Lazanu[30], A. Lebedev[2,1], S. Lebedev[21,1], E. Lebedeva[21], J. Lehnert[2], Y. Leifels[2], Chao Li[31], Qiyan Li[11,35], Xin Li[31], Yuanjing Li[33], V. Lindenstruth[20,2], B. Linnik[11], Feng Liu[35], I. Lobanov[43], E. Lobanova[43], S. Löchner[2], P.-A. Loizeau[2], K. Łojek[4], S.A. Lone[8], J.A. Lucio Martínez[38],Xiaofeng Luo[35], A. Lymanets[2], Pengfei Lyu[33], A. Maevskaya[44], S. Mahajan[24], T. Mahmoud[21], P. Maj[17], Z. Majka[4], A. Malakhov[13], E. Malankin[14], D. Malkevich[10], O. Malyatina[14], H. Malygina[11,2,32], M. Mandal[7], S. Mandal[7], V. Manko[28], A.M. Marin Garcia[2], J. Markert[2], S. Masciocchi[2], T. Matulewicz[47], L. Meder[15], M. Merkin[16], A. Meyer-Ahrens[19], J. Michel[11], L. Mik[17], K. Mikhailov[10], V. Mikhaylov[48], V. Militsija[32], M.F. Mir[8], D. Miskowiec[2], I. Momot[11,2,32], M.M. Mondal[49], F. Morel[22], T. Morhardt[2], S. Morozov[44], W.F.J. Müller[39,2], C. Müntz[11], S. Mukherjee[3], P. Munkes[19], Yu. Murin[13], C. Nandi[7], E. Nandy[7], L. Naumann[37], T. Nayak[7], V.S. Negi[7], W. Niebur[2], V. Nikulin[45], D. Normanov[14], A. Oancea[38], Kunsu Oh[50], A. Olar[34], Yu. Onishchuk[23], P. Otfinowski[17], E. Ovcharenko[1], S. Pal[7], I. Panasenko[5,32], N.R. Panda[49], S. Parzhitskiy[13], V. Patel[18], C. Pauly[18], D. Peshekhonov[13], V. Petráček[51], M. Petri[11], M. Petriş[12],

A. Petrovici[12], M. Petrovici[12], O. Petukhov[44], D. Pfeifer[18], Hung Pham[22], K. Piasecki[47], J. Pietraszko[2], R. Płaneta[4], V. Plotnikov[10], V. Plujko[23], J. Pluta[29], A. Pop[12], K. Poźniak[29,47], S.K. Prasad[3], M. Prokudin[10], M. Pugach[20,2,32], V. Pugatch[32], S. Querchfeld[18], L. Radulescu[12], S. Raha[3], W. Raja[8], F. Rami[22], J. Rautenberg[18], R. Ray[3], A. Reinefeld[52], A. Reshetin[44], C. Ristea[30], O. Ristea[30], S. Rode[53], A. Rodriguez Rodriguez[2], F. Roether[11], R. Romaniuk[29], A. Rost[42], E. Rostchin[45,14], I. Rostovtseva[10], A. Roy[53], Yu. Ryabov[45], I. Sagdiyev[14], R. Sahoo[53], P.K. Sahu[49], S.K. Sahu[49], J. Saini[7], F. Salem[52], S. Samanta[3], S.S. Sambyal[24], V. Samsonov[45,14,57], O. Sander[15], S. Sarangi[27], S. Sau[26], C. Schiaua[12], F. Schintke[52], C.J. Schmidt[2], H.R. Schmidt[5], T. Schütt[52], H. Schuldes[11], K. Schweda[2], F. Seck[42], I. Selyuzhenkov[2,14], A. Semennikov[10], A. Senger[2], P. Senger[2,11], A. Shabanov[44], A. Shabunov[13], Ming Shao[31], A.D. Sheremetiev[13], Shusu Shi[35], V. Shumikhin[14], O. Shumkin[14], I. Sibiryak[28], B. Sikora[47], C. Simon[36], C. Simons[2], A.K. Singh[27], B.K. Singh[54], C.P. Singh[54], O. Singh[9], V. Singhal[7], P. Sitzmann[11], L. Škoda[51], I. Som[27], D. Soyk[2], D. Stach[37], P. Staszel[4], M. Strikhanov[14], J. Stroth[11,2], C. Sturm[2], R. Sultanov[10], Yongjie Sun[31], D. Svirida[10], O. Svoboda[48], R. Szczygieł[17], Zebo Tang[31], M. Tanha[11], A. Taranenko[14], O. Tarassenkova[45], M.-G. Târzilă[12], M. Teklishyn[39,32], P. Tlustý[48], T. Tölyhi[46], A. Toia[2,11], N. Topil'skaya[44], M. Träger[2], Yu. Tsyupa[43], N.G. Tuturas[30], F. Uhlig[2], E. Usenko[44], I. Valin[22], D. Varga[46], I. Vassiliev[2], O. Vasylyev[2], S. Vinogradov[14], R. Visinka[2], M. Völkl[5], A. Volochniuk[23], A. Vorobiev[43], A. Voronin[16], V. Vovchenko[20], Dong Wang[35], Xi-Wei Wang[40], Yi Wang[33], A.A. Weber[21], M. Weber[15], P. Weidenkaff[36], C. Wendisch[2], J.P. Wessels[19], D. Wielanek[29], A. Wieloch[4], A. Wilms[2], M. Winter[22], Gy. Wolf[46], Sanguk Won[50], Ke-Jun Wu[40], Nu Xu[35], Junfeng Yang[31], Rongxing Yang[31], Zhongbao Yin[35], In-Kwon Yoo[50], Jianhui Yuan[31], I. Yushmanov[28], W. Zabołotny[29,47], Yu. Zaitsev[10], N.I. Zamiatin[13], M. Zhalov[45], Yifei Zhang[31], Yu Zhang[35], Lei Zhao[31], Yüe Zhao[22], Sheng Zheng[40], Daicui Zhou[35], Jian Zhou[31], Jing Zhou[40], Wenxiong Zhou[2], Xianglei Zhu[33], A. Zinchenko[13], M. Żołądź[17], W. Zubrzycka[17], P. Zumbruch[2], M. Zyzak[2]

[1]Laboratory of Information Technologies, Joint Institute for Nuclear Research (JINR-LIT), Dubna, Russia
[2]GSI Helmholtzzentrum für Schwerionenforschung GmbH (GSI), Darmstadt, Germany
[3]Department of Physics, Bose Institute, Kolkata, India
[4]Marian Smoluchowski Institute of Physics, Jagiellonian University, Kraków, Poland
[5]Physikalisches Institut, Eberhard Karls Universität Tübingen, Tübingen, Germany
[6]Department of Physics, Panjab University, Chandigarh, India
[7]Variable Energy Cyclotron Centre (VECC), Kolkata, India
[8]Department of Physics, University of Kashmir, Srinagar, India
[9]Department of Physics, Aligarh Muslim University, Aligarh, India
[10]Institute for Theoretical and Experimental Physics (ITEP), Moscow, Russia
[11]Institut für Kernphysik, Goethe-Universität Frankfurt, Frankfurt, Germany
[12]Horia Hulubei National Institute of Physics and Nuclear Engineering (IFIN-HH), Bucharest, Romania
[13]Veksler and Baldin Laboratory of High Energy Physics, Joint Institute for Nuclear Research (JINR-VBLHEP), Dubna, Russia
[14]National Research Nuclear University MEPhI, Moscow, Russia
[15]Karlsruhe Institute of Technology (KIT), Karlsruhe, Germany
[16]Skobeltsyn Institute of Nuclear Phyiscs, Lomonosov Moscow State University (SINP-MSU), Moscow, Russia
[17]AGH University of Science and Technology (AGH), Kraków, Poland
[18]Fakultät für Mathematik und Naturwissenschaften, Bergische Universität Wuppertal, Wuppertal, Germany
[19]Institut für Kernphysik, Westfälische Wilhelms-Universität Münster, Münster, Germany
[20]Frankfurt Institute for Advanced Studies, Goethe-Universität Frankfurt (FIAS), Frankfurt,

Germany
[21]Justus-Liebig-Universität Gießen, Gießen, Germany
[22]Institut Pluridisciplinaire Hubert Curien (IPHC), IN2P3-CNRS and Université de Strasbourg, Strasbourg, France
[23]Department of Nuclear Physics, Taras Shevchenko National University of Kyiv, Kyiv, Ukraine
[24]Department of Physics, University of Jammu, Jammu, India
[25]Department of Physics, Gauhati University, Guwahati, India
[26]Department of Physics and Department of Electronic Science, University of Calcutta, Kolkata, India
[27]Indian Institute of Technology Kharagpur, Kharagpur, India
[28]National Research Centre "Kurchatov Institute", Moscow, Russia
[29]Institute of Electronic Systems, Warsaw University of Technology, Warsaw, Poland
[30]Atomic and Nuclear Physics Department, University of Bucharest, Bucharest, Romania
[31]Department of Modern Physics, University of Science & Technology of China (USTC), Hefei, China
[32]High Energy Physics Department, Kiev Institute for Nuclear Research (KINR), Kyiv, Ukraine
[33]Department of Engineering Physics, Tsinghua University, Beijing, China
[34]Eötvös Loránd University (ELTE), Budapest, Hungary
[35]College of Physical Science and Technology, Central China Normal University (CCNU), Wuhan, China
[36]Physikalisches Institut, Universität Heidelberg, Heidelberg, Germany
[37]Institut für Strahlenphysik, Helmholtz-Zentrum Dresden-Rossendorf (HZDR), Dresden, Germany
[38]Institute for Computer Science, Goethe-Universität Frankfurt, Frankfurt, Germany
[39]Facility for Antiproton and Ion Research in Europe GmbH (FAIR), Darmstadt, Germany
[40]College of Science, China Three Gorges University (CTGU), Yichang, China
[41]Institut für Technische Informatik, Universität Heidelberg, Mannheim, Germany
[42]Institut für Kernphysik, Technische Universität Darmstadt, Darmstadt, Germany
[43]Institute for High Energy Physics (IHEP), Protvino, Russia
[44]Institute for Nuclear Research (INR), Moscow, Russia
[45]Petersburg Nuclear Physics Institute named by B.P.Konstantinov of National Research Centre "Kurchatov Institute" (PNPI), Gatchina, Russia
[46]Institute for Particle and Nuclear Physics, Wigner Research Centre for Physics, Hungarian Academy of Sciences, Budapest, Hungary
[47]Faculty of Physics, University of Warsaw, Warsaw, Poland
[48]Nuclear Physics Institute of the Czech Academy of Sciences, Řež, Czech Republic
[49]Institute of Physics, Bhubaneswar, India
[50]Pusan National University (PNU), Pusan, Korea
[51]Czech Technical University (CTU), Prague, Czech Republic
[52]Konrad-Zuse-Zentrum für Informationstechnik Berlin (ZIB), Berlin, Germany
[53]Indian Institute of Technology Indore, Indore, India
[54]Department of Physics, Banaras Hindu University, Varanasi, India
[55]also: Institute of Space Science, Bucharest, Romania
[56]also: Technische Universität Dresden, Dresden, Germany
[57]also: St. Petersburg Polytechnic University (SPbPU), St. Petersburg, Russia